8

Multidisciplinary Design Aspects

The design and development approaches of aerospace vehicles of either kind are basically the same as those of conventional aircraft. Their background is given by Cayley's design paradigm. Sir George Cayley (1773–1857) was an early British aviation pioneer who conceived the essentials of the aircraft as we know it today [1]. Paraphrasing Cayley's design paradigm [2, 3]:

- Assign functions plainly to corresponding subsystems, e.g.
  - wing ⇒ provision of lift,
  - propulsion system ⇒ overcoming of drag,
  - horizontal stabilizer and elevator ⇒ longitudinal trim, stabilization and control,
  - vertical stabilizer and rudder ⇒ lateral (directional) stabilization and control,
  - fuselage ⇒ payload accommodation,
  - etc.
- Have the different functions and the corresponding subsystems only weakly and linearly coupled, then you can treat and optimize each function and subsystem more or less independently of the others, but nevertheless treat and optimize the whole aircraft in this way, which integrates all functions and subsystems.

This paradigm has been proven to be very effective (ideally it should hold for every technical apparatus). However, the quest for more performance and efficiency, the opening of new flight-speed domains, etc., has led over the years to higher and higher integrated functions and subsystems, i.e., a weakening of Cayley's design paradigm. Of course, this is different for different kinds of flight vehicles. In each case, this paradigm does not necessarily encompass all major functions and subsystems.

In the context of our considerations it is interesting and important to note that a differentiation similar to that of subsystems and functions has taken place also of the engineering disciplines which are involved in the design and development of flight vehicles.[1] This is natural, and was and is indeed also a

[1] This differentiation also holds for university education and for research at universities and research establishments.

strong technological driving factor. The differentiation of the engineering disciplines, however, had also adverse effects. It led, for instance, to the presently strongly established sequential and iterative design cycles with a weak interaction of the disciplines. It further led in some cases to autonomy drives of disciplines by duplicating (under the euphemism "adaptation") skills and tools of other disciplines, which then often did not participate in the subsequential developments of the mother disciplines. In view of these developments, the meaning of Cayley's design paradigm is expanded to also cover the disciplines, i.e., both the differentiation of functions/sub-systems (first aspect), and of disciplines (second aspect). The significant observation is now, that both aspects of Cayley's design paradigm are, as already indicated, persistently weakening in modern aircraft design, which holds even more for aerospace flight vehicles.

An important issue for aircraft, as well as aerospace vehicles, for the latter especially for CAV's and ARV's, is that with the present design and development approach, the actual quantification of the aerothermo-servoelastic properties of the vehicle's airframe is made only very late in the development process, after the first, already completely defined and developed, airframe has been assembled.[2] Partly, this quantification process extends deep into the flight envelope opening process. Changes—actually "repair solutions"—which must be made of the airframe, if the said properties do not meet the requirements, can be very costly and in any case will likely increase the structural weight of the vehicle.

Similar problems exist with regard to the structures and materials layout of hypersonic vehicles in view of the thermal loads associated with high-speed flight. Thermal protection systems of either kind cost much weight, not to mention maintenance and repair efforts during the vehicle's lifetime. The real performance of a TPS will become apparent only after the first flight(s). Again "repair solutions" to either improve a TPS or to shed unnecessary mass will be costly and time consuming.

All this must be seen in view of the payload fraction (pay load/dry mass) [4]. For the SÄNGER system, this was estimated to be approximately 4.4 per cent (rocket launcher: approximately 2 per cent). Compared to payload fractions of modern transport aircraft of 30 to 45 per cent, these are very small percentages. This means that the design is much more critical for hypersonic space transportation systems than for transonic aircraft. Hence the development risk is very much larger, which must be seen in the context of the very much larger development costs.

A good chance to overcome these problems, basically the weakening of Cayley's design paradigm (first aspect), lies in the fantastic developments of computational simulation, which we have seen for the last two decades [2]. In general, it appears that a strong and nonlinear coupling of functions and subsystems also asks for a strong discipline coupling. But there are also cases, where

[2] The reader is asked to recall in this regard the particular design problems of airbreathing hypersonic vehicles, Section 4.5.4.

a strong disciplines coupling is mandatory, even if functions/sub-systems obey Cayley's design paradigm. The treatment of these design problems in the classical way is partly possible, but often it leads to increasingly large time and cost increments. Design risks can become large, and, especially with very strong functions and subsystems coupling, they can become untenable. The discussion shows that the weakening of Cayley's design paradigm, in both aspects, asks for new approaches. This holds strongly for aerospace vehicles, especially airbreathing aerospace planes, for both space transportation and military purposes.

The continued enormous growth of computer power and the capabilities of information technologies make a post-Cayley design paradigm (integrated design) a viable option. This usually is understood when speaking of multidisciplinary design and optimization. Of course present day design and development is multidisciplinary, however, usually only in the sense, that the parent discipline brings in the other disciplines in terms of simple and partly very approximate methods.

True multidisciplinary design and optimization must overcome the second aspect of Cayley's design paradigm. It must bring together the best suited tools in a strong coupling of the disciplines. The methods of numerical aerodynamics are a key element of such approaches. Large advancements, however, are necessary in flow physics and thermodynamics modeling [5].

Large advancements and new thinking are necessary, too, in structural mechanics. New structure-physics models are necessary in order to permit the influence of joints of all kind (non-linearities, damping), of non-linear deformations (buckling), etc., to be quantified. This is true in particular when static and dynamic aeroelastic properties of the airframe are to be described and optimized with high accuracy and reliability [2]. Actually, a shift from the *perfect-elastic* to the high-fidelity *real-elastic* airframe consideration and modeling is necessary already in the early design phases, and not late in the development process [3]. This also holds analogously for thermal protection, propulsion integration, guidance and control, etc.

8.1 Introduction and Short Overview of the Objectives of Multidisciplinary Design Work

In the last decade, multidisciplinary design methods were motivated by the recognition that the development of such complex systems as aerospace vehicles can no longer be conducted by an isolated treatment of the various components (first aspect of Cayley's design paradigm). The multidisciplinary design process for such vehicles to optimize their performance and missions is very complex. This strictly implies the strong interference between various disciplines (second aspect of Cayley's design paradigm). The global process encom-

passes a technological and an economical part.[3] The technological part consists mainly of the

- aerodynamic shape,
- aerothermodynamic performance including stability, controllability and maneuverability,
- ascent, descent, and contingency trajectories,
- guidance and control concept,
- masses: vehicle, propellants, payload,
- internal lay-out with the definition of the center-of-gravity and the moments of inertia,
- structures and materials layout including thermal protection systems,
- main propulsion system,
- reaction control system.

There exists for every technical system the challenge to deal with a large number of design variables and constraints which come from the disciplines contributing to the definition and synthesis of the system. These contributing disciplines are in general not independent from each other. Some of the interactions between the disciplines are so intense that only a closely coupled consideration of the physical behavior leads to really reliable and valuable results [6, 7].

We do not have the intention here to give a comprehensive survey about all the various methods for dealing with the multidisciplinary design and optimization problem. We shortly address some of the analysis tools [8]. First, however we state that the design variables forming the design space can be classified as entities being

- either continuous, such as the thrust of a rocket as function of the physics of the flow and the material under the condition of minimized side loads,
- or non-continuous (integer, discrete), such as the cost of the design and development of a highly sophisticated space-transportation system.

If the design variables are continuous, gradient-based and search methods are employed. Response-surface methods are used, when the whole vehicle is treated as a system with non-continuous (integer, discrete) design variables. Gradient-based methods should be applied whenever possible since they are much more effective than search methods. Gradient-based methods use the information of the **function derivatives** to locate local extremes. Search methods use only the **function** information to determine a global extreme. In the case that some elements of the design space are non-continuous (mixed-variable design space), gradient-based optimization algorithms are not the methods of choice. Typical disciplines, which do not provide continuous design variables, are material definition, manufacturing, maintenance, and cost determination.

[3] Customarily the main items considered are costs, operations, and rate of return of investment.

Methods are available which are well suited for dealing with mixed-variable design spaces. These are the response-surface methods[4] with approximations based on

- neural networks [9, 10],
- fuzzy logic [11, 12],
- genetic algorithms [13, 14].

A response surface is generated by the experts of the disciplines who treat the single parts (subsystems) of the whole system. Each discipline contributes design solutions for statistically selected combinations of design parameters within the design space. Therefore, the response-surface method generally performs optimization on system level rather than on discipline level.

For example, Fig. 8.1 shows a simplified flow chart of the optimization process for the design of an aerospace vehicle with an inner loop generating a single design point.

We distinguish two interactions between the various disciplines.[5] The first type of interaction is weak, in the sense that the disciplines involved each have a separate physical description. Examples are:

- Steady contour changes of elements of vehicle shape $\Longrightarrow$ change of flow field,
- Change of aerodynamic performance $\Longrightarrow$ change of flight trajectory,
- Change of characteristics of propulsion system $\Longrightarrow$ change of vehicle's flight mechanics.

The second type of interaction is the strong one, where the disciplines involved require a coupled physical description, if advanced technology aspects with new capabilities like enhanced performance, flight safety, reliability and cost effectiveness are taken into account. Examples for that case are:

- Dynamic contour change of elements of vehicle shape due to aerodynamic (mechanical) loads $\Longleftrightarrow$ unsteady change of aerodynamic flow field (aeroelasticity),
- Heat transfer in structures $\Longleftrightarrow$ change of aerothermodynamic flow field (thermal surface effects),
- Contour change of elements of vehicle shape by thermal stresses $\Longleftrightarrow$ deformation of structure and change of aerothermodynamic flow field.

In agreement with the scope of this book we focus now our attention on approaches to describe the second type of interaction, viz. strong interactions.

[4] These methods are also called search methods.

[5] By interaction we mean the mutual influence of physical behavior, i.e., the exchange of physical information. With coupling we mean the mathematical formulation of the exchange of information.

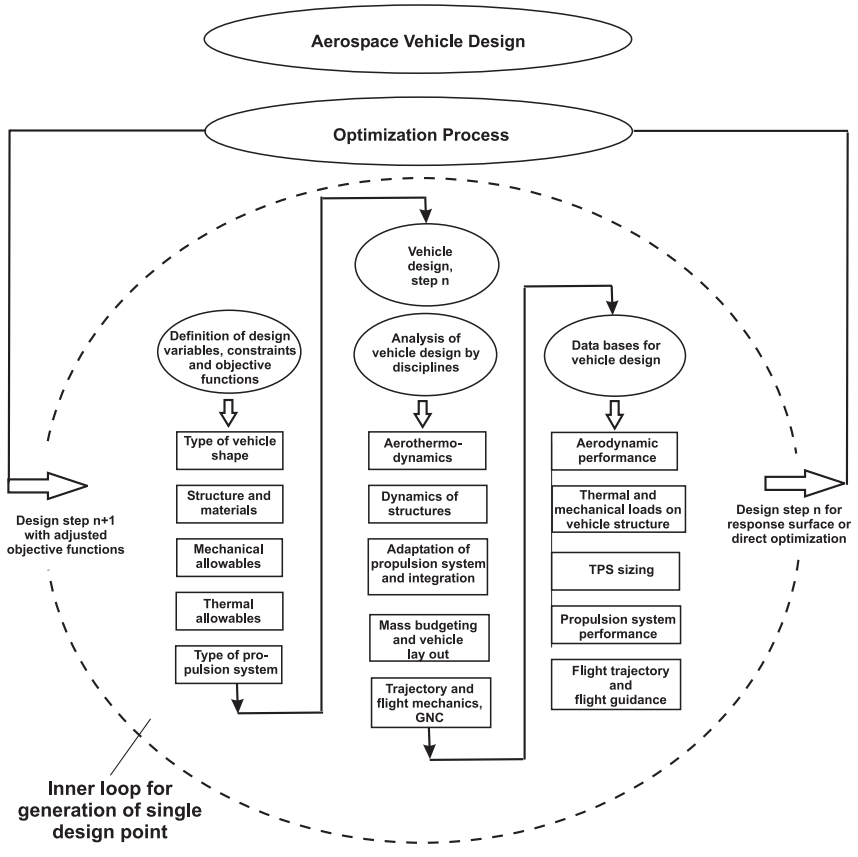

Fig. 8.1. Simplified flow chart illustrating the optimization process for aerospace vehicle design. "Type" denotes, for example the class of an aerospace vehicle, either a capsule or a bicone or a RV-W, and similar for the propulsion system.

8.2 Equations for Fluid-Structure Interaction Domains

8.2.1 Fluid Dynamics Equations

In Appendix A, we present the fluid dynamic equations for unsteady viscous flows in Cartesian coordinates $(x,\ y,\ z)$, eq. (A.1). For flows past elastically deforming configurations (e.g., due to unsteady aerothermodynamic loads), the body surface as "inner" boundary of the flow-computation domain deforms in a time-dependent manner. Due to that, any grid, either structured or unstructured, of the numerical flow solution procedure is also time-dependent. Therefore a coordinate transformation to arbitrary non-orthogonal time-dependent coordinates $(\xi,\ \eta,\ \zeta)$, Fig. 8.2, is the method of choice for dealing with this kind of problems:

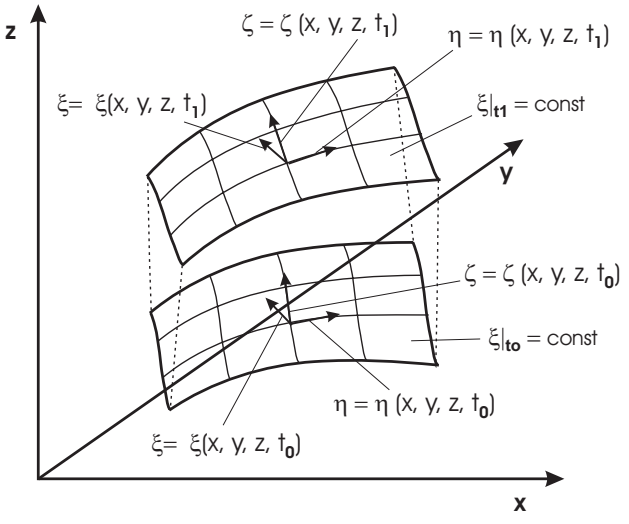

Fig. 8.2. Arbitrary non-orthogonal time-dependent coordinates defining iso-surfaces $\xi = \text{const.}$ at times t_0 and t_1.

$$\begin{aligned} \xi &= \xi(x, y, z, t), \\ \eta &= \eta(x, y, z, t), \\ \zeta &= \zeta(x, y, z, t), \\ \tau &= t. \end{aligned} \tag{8.1}$$

Equation (A.1) then reads

$$\frac{\partial \underline{\hat{Q}}}{\partial \tau} + \frac{\partial(\underline{\hat{E}} - \underline{\hat{E}}_{\,visc})}{\partial \xi} + \frac{\partial(\underline{\hat{F}} - \underline{\hat{F}}_{\,visc})}{\partial \eta} + \frac{\partial(\underline{\hat{G}} - \underline{\hat{G}}_{\,visc})}{\partial \zeta} = 0, \tag{8.2}$$

with

$$\underline{\hat{Q}} = J^{-1}\underline{Q}, \tag{8.3}$$

$$\underline{\hat{E}} = J^{-1}\begin{pmatrix} \rho U \\ \rho u U + \xi_x p \\ \rho v U + \xi_y p \\ \rho w U + \xi_z p \\ (\rho e_t + p)\, U - \xi_t p \end{pmatrix}, \quad \underline{\hat{E}}_{\,visc} = J^{-1}\begin{pmatrix} 0 \\ \xi_x \tau_{xx} + \xi_y \tau_{xy} + \xi_z \tau_{xz} \\ \xi_x \tau_{yx} + \xi_y \tau_{yy} + \xi_z \tau_{yz} \\ \xi_x \tau_{zx} + \xi_y \tau_{zy} + \xi_z \tau_{zz} \\ \xi_x \beta_x + \xi_y \beta_y + \xi_z \beta_z \end{pmatrix},$$

$$\underline{\hat{F}} = J^{-1}\begin{pmatrix} \rho V \\ \rho u V + \eta_x p \\ \rho v V + \eta_y p \\ \rho w V + \eta_z p \\ (\rho e_t + p)\, V - \eta_t p \end{pmatrix}, \quad \underline{\hat{F}}_{visc} = J^{-1}\begin{pmatrix} 0 \\ \eta_x \tau_{xx} + \eta_y \tau_{xy} + \eta_z \tau_{xz} \\ \eta_x \tau_{yx} + \eta_y \tau_{yy} + \eta_z \tau_{yz} \\ \eta_x \tau_{zx} + \eta_y \tau_{zy} + \eta_z \tau_{zz} \\ \eta_x \beta_x + \eta_y \beta_y + \eta_z \beta_z \end{pmatrix}, \tag{8.4}$$

$$\underline{\hat{G}} = J^{-1}\begin{pmatrix} \rho W \\ \rho u W + \zeta_x p \\ \rho v W + \zeta_y p \\ \rho w W + \zeta_z p \\ (\rho e_t + p)\, W - \zeta_t p \end{pmatrix}, \quad \underline{\hat{G}}_{visc} = J^{-1}\begin{pmatrix} 0 \\ \zeta_x \tau_{xx} + \zeta_y \tau_{xy} + \zeta_z \tau_{xz} \\ \zeta_x \tau_{yx} + \zeta_y \tau_{yy} + \zeta_z \tau_{yz} \\ \zeta_x \tau_{zx} + \zeta_y \tau_{zy} + \zeta_z \tau_{zz} \\ \zeta_x \beta_x + \zeta_y \beta_y + \zeta_z \beta_z \end{pmatrix},$$

$$\begin{aligned} \beta_x &= u\tau_{xx} + v\tau_{xy} + w\tau_{xz} - q_x, \\ \beta_y &= u\tau_{yx} + v\tau_{yy} + w\tau_{yz} - q_y, \\ \beta_z &= u\tau_{zx} + v\tau_{zy} + w\tau_{zz} - q_z. \end{aligned} \tag{8.5}$$

Here $J^{-1} = \left|\dfrac{\partial(x,y,z,t)}{\partial(\xi,\eta,\zeta,\tau)}\right|$ is the determinant of the Jacobian matrix of the geometry.

Note that the Cartesian derivatives of the velocity components in the definition of τ_{ij} are transformed using the chain rule. The contravariant velocities are defined by [15]

$$\begin{aligned} U &= \xi_t + \xi_x u + \xi_y v + \xi_z w, \\ V &= \eta_t + \eta_x u + \eta_y v + \eta_z w, \\ W &= \zeta_t + \zeta_x u + \zeta_y v + \zeta_z w. \end{aligned} \tag{8.6}$$

Another form of eq. (8.6) is given by

$$U = \xi_x(u - x_\tau) + \xi_y(v - y_\tau) + \xi_z(w - z_\tau), \tag{8.7}$$

and similarly for V and W, where (x_τ, y_τ, z_τ) are the Cartesian components of the grid velocity.

In the literature [16]–[19], the following form of the Navier–Stokes equations is often used

$$\begin{aligned} \frac{\partial(J^{-1}\underline{Q})}{\partial t} + J^{-1}\left(\frac{\partial(\underline{E} - x_\tau \underline{Q})}{\partial x} + \frac{\partial(\underline{F} - y_\tau \underline{Q})}{\partial y} + \frac{\partial(\underline{G} - z_\tau \underline{Q})}{\partial z}\right) = \\ = J^{-1}\left(\frac{\partial \underline{E}_{visc}}{\partial x} + \frac{\partial \underline{F}_{visc}}{\partial y} + \frac{\partial \underline{G}_{visc}}{\partial z}\right), \end{aligned} \tag{8.8}$$

which is identical to eq. (8.2). Equation (8.2) combined with eq. (8.7) as well as eq. (8.8) is named the arbitrary Lagrange-Euler formulation (ALE), which

means that grid points move with velocities other than the velocity of the local fluid element.[6]

8.2.2 Structure Dynamics Equations

The main task of an analysis of a structural system consists in the calculation of the deformations and stresses due to externally applied mechanical and thermal loads. In the theory of elasticity, considering a linear orthotropic material, the relationship between stresses and strains is given by [20]

$$\underline{\sigma} = D(\underline{\varepsilon} - \underline{\varepsilon}_T - \underline{\varepsilon}_I), \tag{8.9}$$

with $\underline{\sigma}$ denoting the stresses, D the elasticity matrix containing the appropriate material properties, $\underline{\varepsilon}$ the resulting strains, $\underline{\varepsilon}_T$ the thermal strains, and $\underline{\varepsilon}_I$ the initial strains. Further we have:

$$\underline{\sigma} = \begin{pmatrix} \sigma_{xx} \\ \sigma_{yy} \\ \sigma_{xx} \\ \sigma_{xy} \\ \sigma_{yz} \\ \sigma_{zx} \end{pmatrix}, \; \underline{\varepsilon}_I = \begin{pmatrix} \varepsilon_{Ixx} \\ \varepsilon_{Iyy} \\ \varepsilon_{Izz} \\ \varepsilon_{Ixy} \\ \varepsilon_{Iyz} \\ \varepsilon_{Izx} \end{pmatrix}, \; \underline{\varepsilon}_T = \begin{pmatrix} \alpha_{xx} \\ \alpha_{yy} \\ \alpha_{zz} \\ 0 \\ 0 \\ 0 \end{pmatrix} \Delta T, \tag{8.10}$$

$$\underline{\varepsilon} = \begin{pmatrix} \varepsilon_{xx} \\ \varepsilon_{yy} \\ \varepsilon_{xx} \\ \varepsilon_{xy} \\ \varepsilon_{yz} \\ \varepsilon_{zx} \end{pmatrix} = \begin{pmatrix} \frac{\partial}{\partial x} & 0 & 0 \\ 0 & \frac{\partial}{\partial y} & 0 \\ 0 & 0 & \frac{\partial}{\partial z} \\ \frac{\partial}{\partial y} & \frac{\partial}{\partial x} & 0 \\ 0 & \frac{\partial}{\partial z} & \frac{\partial}{\partial y} \\ \frac{\partial}{\partial z} & 0 & \frac{\partial}{\partial x} \end{pmatrix} \begin{pmatrix} u \\ v \\ w \end{pmatrix} = S\underline{u}, \tag{8.11}$$

where $\underline{u} = (u,\ v,\ w)^T$ are the displacements, $\underline{\alpha} = (\alpha_{xx},\ \alpha_{yy},\ \alpha_{zz},\ 0,\ 0,\ 0)^T$ the thermal expansion coefficients, and $\Delta T = T - T_{ref}$ is the temperature difference.[7]

The equilibrium condition $S^T\underline{\sigma} + \underline{b} = 0$, saying that the internal forces have to be equal to the external forces (body forces) in connection with the principle of virtual work, leads to the relation [21]

$$\int_V \delta\underline{\varepsilon}^T \underline{\sigma}\, dV - \int_V \delta\underline{u}^T \underline{b}\, dV - \int_S \delta\underline{u}^T \underline{t}\, dS - \sum_a \delta\underline{u}_a^T \underline{f}^a = 0, \tag{8.12}$$

with $\delta\underline{\varepsilon}$ being the virtual strains, $\delta\underline{u}$ the virtual displacements, $\underline{b}$ the body forces, $\underline{t}$ the tractions (e.g. flow shear stress) on the surface, and $\underline{f}^a$ the single

[6] If the grid point moves with the fluid element, this is called a Lagrange formulation. If the grid point does not move, while the fluid element travels through the grid, we speak of an Euler formulation.

[7] In order to avoid confusion, we note that T, used as superscript in this and the next sub-section, denotes the transpose of the corresponding vector or matrix.

forces at nodal points a. Transferring eq. (8.12) to a finite element formulation, the integrals are divided to yield sums over individual elements 'e'

$$\sum_e \int_{V^e} \delta\underline{\varepsilon}^T D(\underline{\varepsilon} - \underline{\varepsilon}_T - \underline{\varepsilon}_I)\, dV - \sum_e \int_{V^e} \delta\underline{u}^T \underline{b}\, dV - \\ - \sum_e \int_{S^e} \delta\underline{u}^T \underline{t}\, dS - \sum_a \delta\underline{u}_a^T \underline{f}^a = 0. \tag{8.13}$$

We now apply the usual assumptions of finite element theory [21, 22], namely that the displacements in an element are defined by the displacements $\underline{\tilde{u}}$ at the nodes of this element

$$\delta\underline{u} = \sum_a \underline{N}_a\, \delta\underline{\tilde{u}}_a \equiv \underline{N}\, \delta\underline{\tilde{u}}, \tag{8.14}$$

and that the strains are formulated by

$$\delta\underline{\varepsilon} = \sum_a S\underline{N}_a\, \delta\underline{\tilde{u}}_a = \sum_a \underline{B}_a\, \delta\underline{\tilde{u}}_a \equiv \underline{B}\, \delta\underline{\tilde{u}}, \tag{8.15}$$

where $\underline{N}_a$ are the shape functions at the nodal point a. Then with eq. (8.13) we obtain

$$\sum_e \delta\underline{\tilde{u}}_a^T \left(\int_{V^e} \underline{B}_a^T D\, (\underline{B}_b \underline{\tilde{u}}_b - \underline{\alpha}\Delta T - \underline{\varepsilon}_I)\, dV - \right. \\ \left. - \int_{V^e} \underline{N}_a^T \underline{b}\, dV - \int_{S^e} \underline{N}_a^T \underline{t}\, dS - \underline{f}^a \right) = 0. \tag{8.16}$$

The displacements $\delta\underline{\tilde{u}}_a$ and $\underline{\tilde{u}}_b$ at the nodal points are independent from the integration variable and can be written outside of the integrals. With

$$K\underline{\tilde{u}} = \underline{F}, \tag{8.17}$$

we find

$$K = \sum_e \int_{V^e} \underline{B}^T D \underline{B}\, dV,$$

and

$$\underline{F} = \sum_e \int_{V^e} \underline{B}^T D\underline{\alpha}\, \Delta T dV + \sum_e \int_{V^e} \underline{B}^T \underline{\varepsilon}_I\, dV + \\ + \sum_e \int_{V^e} \underline{N}^T \underline{b}\, dV + \sum_e \int_{S^e} \underline{N}^T \underline{t}\, dS + \underline{f}. \tag{8.18}$$

In the above, K is called the stiffness matrix and $\underline{F}$ the load vector. Equation (8.17) describes the static equilibrium of a structural system [21].

In cases where the loads change rapidly with time, inertial forces as well as damping forces due to energy dissipation inside the material (e.g. microstructure movement) need to be considered. Replacing in eq. (8.17) the body force $\underline{b}$ by $\bar{\underline{b}} - \rho\ddot{\underline{u}} - \mu\dot{\underline{u}}$ yields

$$M\ddot{\underline{\tilde{u}}} + C\dot{\underline{\tilde{u}}} + K\underline{\tilde{u}} = \underline{F}, \tag{8.19}$$

with the mass matrix

$$M = \sum_e \int_{V^e} \rho \underline{N}^T \underline{N} dV,$$

and the damping matrix[8]

$$C = \sum_e \int_{V^e} \mu \underline{N}^T \underline{N} dV.$$

Equation (8.19) represents the mathematical formulation for the dynamic behavior of elastic structures, however with homogenous damping properties. This points to the difficulty to describe *real-elastic* structures with point- and line-wise distributed joints (rivets, screws, gluing and welding zones), which introduce non-linearities and damping, and of non-linear deformations, as discussed shortly in the opening remarks of this chapter. If these could be modelled to the needed degree, the *real-elastic* properties of a structure could be determined in the design and development process of a flight vehicle much earlier than is currently possible [2].

However, this topic presents enormous challenges. Scale discrepancies as large as in flow with turbulent boundary layers past entire configurations would have to be mastered. It is not clear yet how to proceed. Possible approaches may use statistical models based on parameter identification as in statistical turbulence theory, combined with methods similar to direct numerical or large-eddy simulations. It appears therefore, that the classical approach of structural mechanics based on the computational determination only of the *perfect-elastic* properties, combined with structural tests late in the development process to find the *real-elastic* properties, has to be kept for quite some time.

8.2.3 Heat Transport Equation

The thermal energy equilibrium in a solid or fluid can be expressed by the diffusive equation[9]

$$\rho c \frac{\partial T}{\partial t} + \nabla^T \underline{q} - \Omega = 0, \tag{8.20}$$

with ρ the density, c the specific heat, $\underline{q} = -k\nabla T$ Fourier's law of heat conduction,[10] k the thermal conductivity matrix and Ω the internal heat generation.

---

[8] This derivation assumes that the resistance is linear to the velocity $\dot{\underline{\tilde{u}}}$.

[9] Unsteady heat conduction equation.

[10] For the generalized aerothermodynamic heat transfer formulation, see, e.g., [5].

Using the principle of virtual temperatures (which acts in the same way as the virtual displacements), the Gauss' integral theorem and the proper considerations of boundary conditions, the finite element equilibrium equation for heat transport on the basis of eq. (8.20) has the form [20, 23]

$$\underbrace{\int_V \rho c \underline{N}^T \underline{N} dV}_{C} \dot{\mathbf{T}} + \underbrace{\int_V \underline{B}^T \lambda \underline{B}\, dV}_{K_c} \mathbf{T} + \underbrace{\int_{Sh} h \underline{N}^T \underline{N} dS}_{K_h} \mathbf{T} = \tag{8.21}$$

$$\underbrace{\int_V \Omega \underline{N}^T dV}_{P_\Omega} + \underbrace{\int_{Ss} q_s \underline{N}^T dS}_{P_q} + \underbrace{\int_{Sh} h T_e \underline{N}^T dS}_{P_h} - \underbrace{\int_{Sr} \hat{\sigma} \epsilon \, (T_s^4 - T_a^4) \underline{N}^T dS}_{P_r},$$

where the following boundary conditions are applied[11]

$\underline{q} \cdot \underline{n} = -q_s$	specified surface heat flow on S_s,
$\underline{q} \cdot \underline{n} = h\,(T_s - T_e)$	convective heat exchange on S_h,
$\underline{q} \cdot \underline{n} = \hat{\sigma} \epsilon\, (T_s^4 - T_a^4)$	radiation heat exchange on S_r.

In eq. (8.21), $\mathbf{T}$ is the element nodal temperature vector and $\dot{\mathbf{T}}$ the time derivative of $\mathbf{T}$, T_s the surface temperature, T_e the temperature at the boundary layer edge, T_a the ambient temperature, h the convective heat transfer coefficient (see Section 10.3), $\hat{\sigma}$ the Stefan–Boltzmann constant[12] and ϵ the emission coefficient. Equation (8.21) can be written in matrix form:

$$C\, \dot{\mathbf{T}} + (K_c + K_h)\, \mathbf{T} = P_\Omega + P_q + P_h - P_r = \mathbf{P}\,, \tag{8.22}$$

with C being the heat capacity matrix, K_c the conduction matrix and K_h the convection matrix. The vector $\mathbf{P}$ contains the heat inputs arising from several sources defined above and the heat radiation from the surface.[13]

8.3 Coupling Procedures

The main problem for disciplines analyzing physical states which interact strongly with each other is that they have to provide for a fast and precise exchange (or transfer) of data at the corresponding boundaries, in the way that

[11] Generally the surfaces S_s, S_h and S_r are different, but in some specific application cases we may have $S_s \equiv S_h \equiv S_r$.

[12] The symbol for the Stefan–Boltzmann constant with the circumflex $\hat{\sigma}$ is used here in order to distinguish it from the symbol of the stresses σ.

[13] In case of concave contours, the heat radiation depends on the local view factor (non-convex effects, Section 9.1) which describes for a given surface element the ratio of heat emission and absorption and leads to an adjustment of P_r [22, 23].

an equilibrium state, either static or quasi-static (dynamic), is achieved.[14] The coupling of the solutions of various disciplines is easiest and provides best results, if in the different domains the same kind of numerical approximation methods (e.g., finite element methods) as well as conformal meshes (e.g., unstructured grids) along the common boundaries are used. This has the consequence that at most an interpolation in the frame of the, e.g., finite element solution during the data transfer at the boundaries has to be conducted. But in real applications this is often not practical, since in general the fluid domain needs a finer grid resolution than the structural domain and the solution procedure itself (e.g., FEM) is not always appropriate for integrating the fluid dynamical equations, in particular in the hypersonic regime.

Therefore in the past few years, it could be observed that methods were developed which are based in each case on the best approximation in the corresponding application domain. This has some advantages. First, methods for the various disciplines can be used, which are well tested and verified, which also includes commercial products in particular for the structural domain. Secondly, the grid can be more precisely adapted where it is required by the physics. It might be in one domain unstructured and in another domain structured as best suited to the solution method employed. However, the disadvantage consists in the more complex data transfer across the common interface boundary, which requires a special treatment, since in general a sophisticated interpolation method is necessary.

The coupling process depends strongly on the physical situation to be solved. For example, the requirements on the solution process for an aeroelastic problem are quite different from those of a heat transfer problem. Our main interest here consists in describing the coupling procedure for fluid–heat transfer problems (thermal fluid-structure interaction). Nevertheless we will address also some other applications like aeroelasticity (mechanical fluid-structure interaction), ablation, etc. We begin with the description of the *mechanical-fluid structure interaction* (classical aeroelastic approaches), look then at the *thermal-fluid structure interaction* (without structural response) and finally at the *thermal-mechanical fluid-structure interaction* (with structural response).

8.3.1 Mechanical Fluid–Structure Interaction Aeroelastic Approach I

For the treatment of the aeroelastic problem, over the years, the authors of [24] to [29] have introduced a specific system of methods. Therein, both the equations for the dynamic structural motion and for fluid dynamics are approximated and solved by a finite element approach. Used are the fluid dynamic equations in the Euler formulation, eq. (A.1), where no grid movement is incorporated. As already mentioned, the data transfer between the disciplines

[14] We consider here only solutions based on numerical methods for fluid dynamics (CFD) and for structural dynamics (CSD).

along the common boundary is simplified by employing a monolithic approach. Since the unsteady CFD Euler method needs very significant computer time, a system-identification procedure was developed, based on some unsteady master CFD solutions for provision of the unsteady aerodynamic loads, which are required in the dynamic structural solver, eq. (8.19), where $F = f_a(t)$ represents the unsteady aerodynamic loads.

8.3.2 Mechanical Fluid–Structure Interaction Aeroelastic Approach II

Another strategy for the treatment of aeroelastic problems was pursued by the authors of [16]–[19],[30]–[32]. They consider besides the fluid and structure fields the moving mesh as a third field. The corresponding equations for the three fields have to be solved simultaneously.

The set of equations is compiled by the semi-discrete form of eq. (8.8) or eq. (8.2) for fluid dynamics, which could, for example, be approximated by a finite-volume approach by eq. (8.19) for structural dynamics, and by

$$\tilde{M}\ddot{\underline{x}} + \tilde{C}\dot{\underline{x}} + \tilde{K}\underline{x} = K_t\tilde{\underline{u}} \tag{8.23}$$

for the moving mesh, where $\underline{x}$ describes the position of a moving fluid grid point. $\tilde{M}, \tilde{C}, \tilde{K}$ are fictitious mass, damping and stiffness matrices, respectively, and K_t is designed as transfer matrix describing the continuity between structural displacement and moving fluid mesh along the common interface boundary.

The coupling of the fluid and structure equations at the interface boundary Γ is conducted by imposing:

$$\begin{aligned} \sigma_S \cdot \underline{n} &= -p\,\underline{n} + \sigma_F \cdot \underline{n}, \\ \frac{\partial \underline{u}_S}{\partial t} &= \frac{\partial \underline{u}_F}{\partial t} && \text{no-slip condition,} \\ \frac{\partial \underline{u}_S}{\partial t} \cdot \underline{n} &= \frac{\partial \underline{u}_F}{\partial t} \cdot \underline{n} && \text{slip condition,} \end{aligned} \tag{8.24}$$

with σ_S, σ_F the tensors of structural and fluid viscous stresses, $\underline{u}_S$, $\underline{u}_F$ the displacements of the structural and fluid fields, p the fluid pressure field and $\underline{n}$ the normal on a given point on Γ. Further the coupling between the structure and the moving grid on Γ takes place via the relations:

$$\begin{aligned} \underline{x} &= \underline{u}_S, \\ \frac{\partial \underline{x}}{\partial t} &= \frac{\partial \underline{u}_S}{\partial t}. \end{aligned} \tag{8.25}$$

For accuracy, stability and convergence reasons the solution of eq. (8.23) must meet the so called geometric conservation law, which can be achieved by an appropriate time discretization of the time-dependent grid position $\underline{x}$ representing the mesh velocity $\dot{\underline{x}}$, [16].

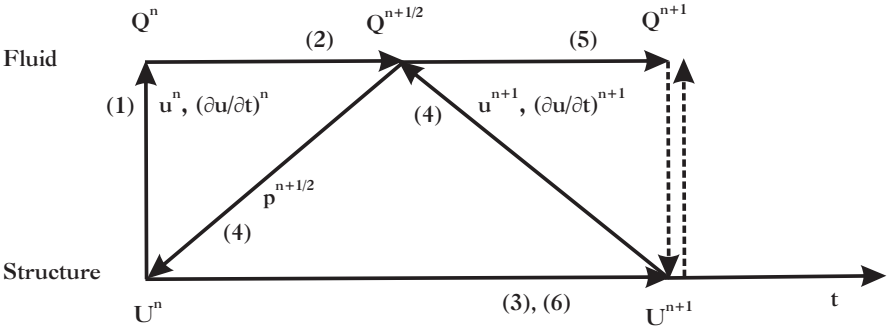

Fig. 8.3. Staggered scheme with inter-field parallelism for the coupling of the solutions of a three-fields fluid-structure interaction problem, $U = (u, \dot{u})^T$ [33].

The three-fields approach allows for the employment of the partitioned solution procedure, where best suited numerical simulation methods can be applied for the various disciplines, like finite-volume or finite-difference methods in the fluid domain and finite element methods in the structural and moving mesh domains.

A solution strategy, regarding the time coupling for the set of the coupled equations (8.8), (8.19), (8.23), with a powerful capacity concerning the numerical stability and the accuracy of the results, is given by the staggered scheme, Fig. 8.3 [33]. This scheme can be described by

1. update the fluid mesh coordinates with structural displacements u^n and the velocities $\dot{u}^n$ to conform to the structural boundary at t^n,
2. advance the flow from t^n to $t^{n+1/2}$,
3. advance the structure using the pressure and the stress field at t^n from t^n to t^{n+1},
4. transfer the pressure and the stress field at $t^{n+1/2}$ to the structural code and transfer the structural displacements u^{n+1} and the velocities $\dot{u}^{n+1}$ to the fluid code,
5. advance the flow from $t^{n+1/2}$ to t^{n+1},
6. re-compute the structure using the pressure and the stress field at $t^{n+1/2}$ from t^n to t^{n+1}.

The above procedure is a variation of the scheme reported in [18], which was also successfully used for space applications [34].

In general the mesh applied to the structural system is coarser than the mesh required for a proper resolution of the fluid domain. This means that typically the common boundaries Γ of the fluid and structural domains have non-matching discrete interfaces. Therefore, the transfer of the displacements from the structural domain to the fluid mesh as well as the transfer of the pres-

sure and stress field to the structural mesh can be critical with respect to consistency and load conservation.[15]

A promising approach to solving this problem, sometimes indicated as the space-coupling strategy, is given in [19]. The main idea behind it is the definition of Gauss points on the finite elements, which are in contact with the structural boundary interface Γ_S, and the connection of these with appropriate cells or elements of the fluid boundary interface Γ_F, in the sense to provide these points with the pressure and the shear stress field values of the fluid. This procedure is known as "pairing" and several algorithms are available for solving this task [35, 36].

A similar approach is reported in [37], where a neutral interface, defined by two Gauss parameters, is constructed, which acts as data-transfer medium between the boundary interfaces[16] Γ_S and Γ_F. These procedures are often used for practical applications conducted by the aerospace industry [39]–[41].

8.3.3 Thermal–Mechanical Fluid–Structure Interaction

One of the earliest if not the first paper dealing with the simulation of coupled thermal–mechanical fluid–structure interaction is [42] from the year 1988. There a monolithic finite element environment was developed for solving the Navier–Stokes equations for the flow field, the structural equations for the mechanical response and the heat conduction equation for the thermal field in the solid. Further the finite element grids, created for the flow and the structure field, had at the common interface the same nodes which render any interpolation for transferring the boundary conditions unnecessary.

Generally, supersonic and hypersonic flows past RV-W's and RV-NW's, as well as CAV/ARV's, heat up the—in general radiation-cooled—surface material of the vehicles. This has two major consequences. First, the structure responds to the severe surface temperature with thermal stresses and/or deformations. Secondly, responding to the severe thermal state of the surface—that are the surface-temperature and the temperature gradients in the gas at the wall, Chapter 9—and the deformation, the general properties of the flow field (e.g. thermal surface effects, shock waves, expansion zones, local separation with vortex phenomena, etc.) and the properties of the thermal boundary layer may change dramatically. Therefore for an advanced design of aerospace vehicles coupled solutions of the corresponding disciplines are indispensable.

In the more general case, where thermal–mechanical fluid–structure interactions with moving grids are considered, the set of governing equations consists of

[15] Load conservation is considered here in the sense that the forces and energies (for example displacement work) on the fluid/structure interface Γ, evaluated by a suitable interpolation procedure, are consistent.

[16] Another interesting solution regarding the data transfer between non-matching boundaries can be found in [38]. There, the construction of a virtual grid is proposed, which has a similar function as the neutral interface mentioned above.

– the Navier–Stokes equations in ALE-formulation for the flow field, eq. (8.2) or (8.8),
– the finite element representation of structure dynamics, eq. (8.19),
– the finite element representation of the heat conduction in solids, eq. (8.22),
– the finite element representation for the moving mesh, eq. (8.23).

This is a four-fields approach in the sense described also in [31]. Another approach, where the determination of the moving mesh by eq. (8.23) is replaced by various mesh tracking procedures, is reported in [43]. For RV-W's and RV-NW's, often the deformations due to thermal and mechanical (pressure and stress field) loads are small. This is the reason why the investigations reported in [23],[44]–[46] do not include a moving mesh capability in the fluid domain.

To include the thermal conditions, the interface boundary conditions on Γ as formulated for the aeroelastic case, eqs. (8.24) and (8.25), have to be extended. They consist now of

- the structural compatibility conditions, eq. (8.24):

$$\begin{aligned} \sigma_S \cdot \underline{n} &= -p\,\underline{n} + \sigma_F \cdot \underline{n}, \\ \frac{\partial \underline{u}_S}{\partial t} &= \frac{\partial \underline{u}_F}{\partial t} && \text{no-slip condition,} \\ \frac{\partial \underline{u}_S}{\partial t} \cdot \underline{n} &= \frac{\partial \underline{u}_F}{\partial t} \cdot \underline{n} && \text{slip condition,} \end{aligned}$$

- the temperature continuity and heat flux equilibrium conditions:

$$\begin{aligned} \lambda_S \nabla T_S \cdot \underline{n} &= \lambda_F \nabla T_F \cdot \underline{n}, \\ T_S &= T_F, \end{aligned} \tag{8.26}$$

- the mesh motion continuity conditions, eq. (8.25):

$$\begin{aligned} \underline{x} &= \underline{u}_S, \\ \frac{\partial \underline{x}}{\partial t} &= \frac{\partial \underline{u}_S}{\partial t}. \end{aligned}$$

As already indicated, for aeroelastic problems the evolution with respect to the development of simulation systems for thermal–mechanical fluid–structure interaction issues exhibits, that loosely coupled strategies are favored. This allows the combination of independent numerical methods for the single disciplines as well as the application of different grid structures.

One promising method for solving the system of coupled equations (8.8), (8.19), (8.22), (8.23), is to use a staggered scheme,[17] similar to that shown Fig. 8.3. We present here the one proposed in [31] which is called the conventional serial staggered procedure (CSS), Fig. 8.4. For pure fluid–thermal coupling (without mechanical response due to thermal loads) a similar staggered

[17] This is applicable only for transient problems, where the thermal behavior is transient and the mechanical and fluid behaviors are stationary.

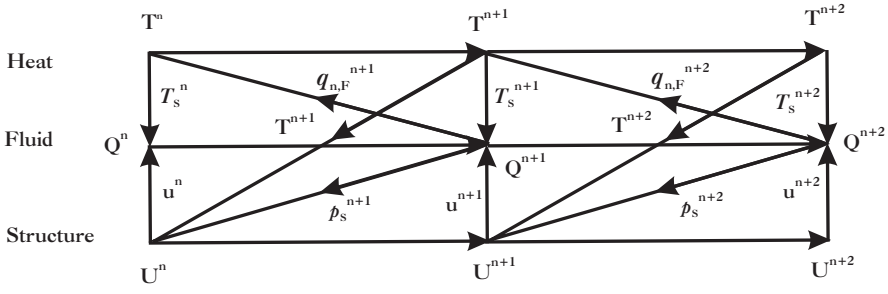

Fig. 8.4. Conventional serial staggered scheme (CSS) for the coupling of the solutions of thermal-mechanical fluid-structure interaction problems [31].

scheme can be found in [45, 47]. Another practical scheme for solving the system of coupled equations is the classical Dirichlet–Neumann iteration which can be applied also for dynamic thermal–mechanical fluid–structure interactions [47, 48]. This scheme consists of the sequence of flux calculations on the interface boundary Γ_F by the fluid equations and the state calculations on the interface boundary Γ_S by the thermal–structural equations. Dirichlet boundary conditions are used in the fluid domain ($\underline{u}$, $\dot{\underline{u}}$, T), and Neumann conditions in the structural domain (q_n, $p \cdot \underline{n}$, $\sigma_F \cdot \underline{n}$).

Let the state in the structural field be denoted by Ψ, which contains deformations and temperatures, and the state at the structural interface boundary Γ_S by Ψ_S, then the iteration for $k+1$ is performed by [44, 47]:

$$\Psi_S^{k+1} = \omega\, \Psi_S^k + (1-\omega)\, \Psi_S^k, \tag{8.27}$$

with the relaxation coefficient $\omega \leq 1$. The iteration has succeeded if a prescribed convergence limit is satisfied.

The other question is how to transfer the data on the interface boundary Γ from one domain to the other, when the grid nodes on the fluid and structure domain do not coincide (non-matching meshes). This is supported by the fact that normally the grid spacing on the fluid side is finer compared to that of the structural side. So the need for an interpolation procedure arises, with the ability to conserve, for example, the sum of loads[18] (pressure and shear stress field) as well as the energy in terms of the heat fluxes along the common interface boundary.

A first possibility of performing the load transfer is given by introducing the Lagrange multipliers δ_i and an additional state variable z, whereby the homogeneity of the virtual work (or virtual power) is preserved, which leads to the relation [49]

[18] Conservation is satisfied if the sum of loads on the interface boundary of the structure Γ_S is equal to the sum of loads on the interface boundary of the fluid Γ_F.

$$\int_{\Gamma} \delta_i \left(\Psi_i - z\right) d\Gamma = 0, \qquad i = F, S. \tag{8.28}$$

In order to simplify the procedure, one can choose $z = \Psi_S|_\Gamma$, reducing the number of Lagrange multipliers δ_i to one, which makes the numerics easier.

A second method is given by the definition of a virtual surface grid, where the interface boundaries Γ_S and Γ_F are projected to this surface, which is described by two Gauss parameters [37, 43]. Once the virtual surface is constructed, conventional interpolation routines are used for transferring the data from one interface boundary to the other, but this procedure is not in a fully conservative fashion.

A third method is based on the conservation of energy[19] for both the conversion of the fluid pressure and the shear stress fields into a mechanical load and the transfer of the heat fluxes to the structural interface boundary Γ_S [31].

Recent investigations apply the commercial interpolation software MpCCI (Mesh-based parallel Code Coupling Interface), [50]. The standard technique of the commercial MpCCI software can be perceived as a particular formulation of the Lagrange multiplier method and is therefore conservative [23, 45, 48]. In addition this software package includes non-conservative interpolation routines.

8.4 Examples of Coupled Solutions

8.4.1 Mechanical Fluid-Structure Interaction Aeroelastic Approach I

The method described in Sub-Section 8.3.1 was tested and applied to some aerospace vehicle shapes like the X-33 re-entry vehicle, Fig. 8.5, and NASA's generic hypersonic vehicle (GHV), which looks similar to the lower stage of the German SÄNGER wing-body configuration, Fig. 8.6 [51]. A typical result is plotted in Fig. 8.7, where the shape of the first symmetric bending mode is shown.

8.4.2 Mechanical Fluid–Structure Interaction Aeroelastic Approach II

The results obtained in the UNSI project of the European Union, performed in the years 1998–2000, are presented in [39]. In UNSI several contributors employed methods like the ones described in Sub-Section 8.3.2. Some of the results are presented below.

[19] For the pressure and shear stress field the virtual displacement work is considered, whereas for the thermal loads the integral of the heat fluxes over the interface boundaries is used, which has the dimension of a power, $[\mathrm{ML}^2/\mathrm{t}^3]$.

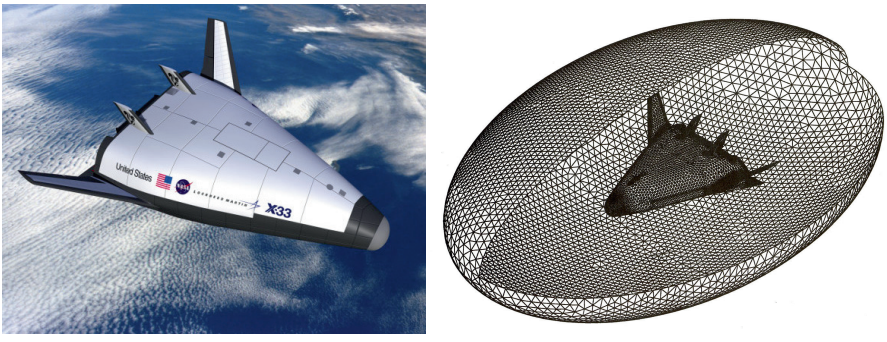

Fig. 8.5. X-33 re-entry vehicle shape (left), and unstructured mesh for a finite element fluid dynamics solver (right) [20].

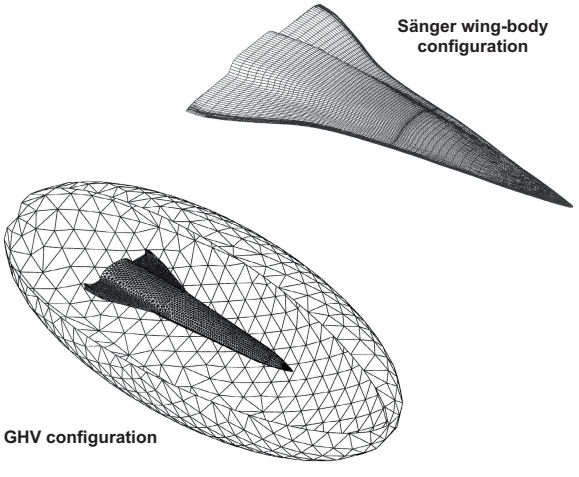

Fig. 8.6. Generic hypersonic vehicle (GHV) configuration with the unstructured finite element mesh for a fluid dynamics solver (lower left), [20]. Wing-body combination with the structured finite-volume surface mesh of the German SÄNGER lower stage configuration (upper right) [51].

We start with results of a study of the AMP wing,[20] which was designed jointly by AEROSPATIALE, DASA, DLR and ONERA in 1990 with the goal to undertake flutter studies for a modern aircraft in the transonic flight regime. There exists a broad experimental data base from investigations in ONERA's S2 wind tunnel in Modane. Every aeroelastic simulation (static or dynamic) of a wing configuration needs as initial geometry the so-called jig shape ($\Longrightarrow$ wind-off shape, $n_z = 0$), which differs from the shape designed for cruise con-

[20] AMP $\Longrightarrow$ Aeroelastic Model Program.

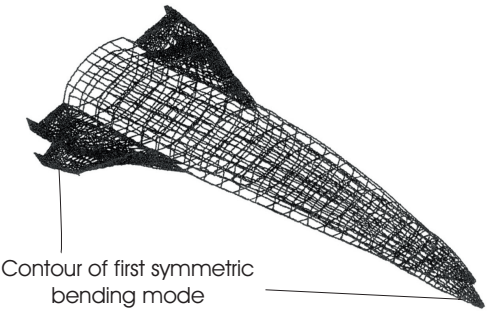

Fig. 8.7. Generic hypersonic vehicle (GHV). Typical structural mode shape: first symmetric bending mode, calculated with the method reported in [24]–[28, 52].

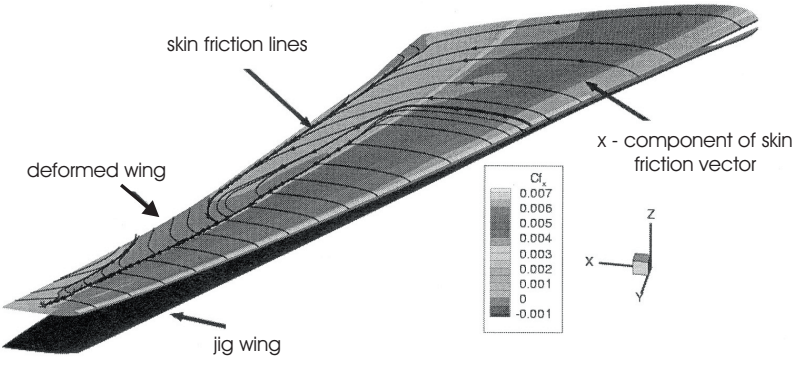

Fig. 8.8. AMP wing: static aeroelastic solution, [39]. Wing deformations and skin-friction lines for $M_\infty = 0.819$, $\alpha = 3.98°$, $Re = 1.99 \cdot 10^6$, $C_L = 0.58$.

ditions.[21] Figure 8.8 shows the static aeroelastic solution of the AMP wing performed with ONERA's inviscid–viscous interaction code VIS25 for the flow and the NASTRAN code for the structure.

The spanwise deformation and the leading edge deflection for another case are shown in Fig. 8.9 where experimental data are compared with data from the VIS25 solver and from ONERA's more sophisticated fluid solver CANARI (unsteady Euler) again coupled with NASTRAN. A moderate overprediction can be observed of the leading edge deflection found with the simulation methods in contrast to the experimental data. This is also true for the wing twist, except at the wing tip, where larger deviations are observed (note the negative coordinate scale in the twist plot.).

[21] The jig shape has the following properties: a) the twist distribution of the design wing is reproduced as a result of a static mechanical fluid-structure simulation at cruise conditions, and b) the vertical locations of the jig wing sections (heights) coincide with the ones of the design wing in the no load case.

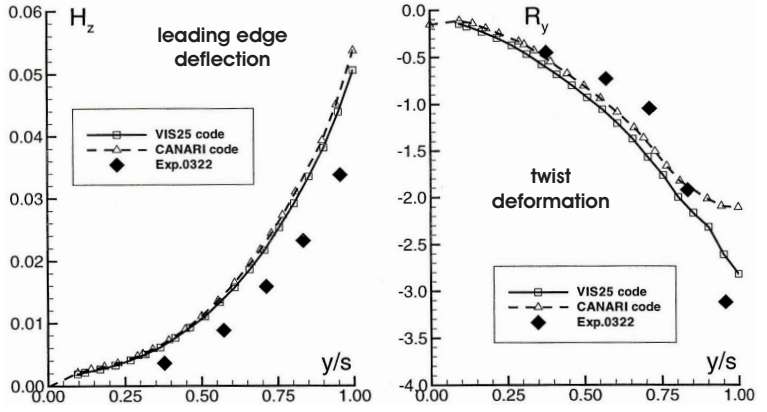

Fig. 8.9. AMP wing: static aeroelastic solution, [39]. Span-wise leading edge deflection H_z and twist deformation R_y. Flow field found with Euler (CANARI) and viscous-inviscid interaction code (VIS25). Comparison with experimental data of the ONERA S2 wind tunnel, Modane. $M_\infty = 0.862$, $\alpha = 1.6°$, $Re = 3.64 \cdot 10^6$, $C_L = 0.3$.

The aeroelastic simulation procedure referred to above with the CANARI code for the flow field is also applied to the coupled dynamic fluid-structure problem. In that case the structural analysis is performed by a modal approach, where the six first mode shapes of the wing are taken into account. In Fig. 8.10, the time evolution of the modal coordinates is displayed for a low transonic test case with $M_\infty = 0.78$, $\alpha = 1.79°$, $Re = 3.49 \cdot 10^6$, $C_L = 0.3$. The stagnation pressure amounts to $p_{stag} = 90$ kPa for which obviously the unsteady responses are damped. This is also true for the first mode, where the damping occurs after a certain time delay, whereas the third mode looks indifferently. Beyond the stagnation pressure of $p_{stag} = 90$ kPa, the modal coordinates are amplified indicating flutter onset.

A second test case, again in the frame of the UNSI project, considers the so called MDO[22] wing–fuselage configuration. This shape was designed in a Brite-Euram project of the EU performed in the years 1996 and 1997. Static aeroelastic computations were conducted by three contributors (two industrial companies, one research institute) using in total eight different methods, including five Euler approaches for the flow field. Figure 8.11 presents a three-dimensional view on the design, the deformed, and the jig shape of the MDO wing as a result of a static aeroelastic solution.

The quality of today's simulation capacity for aeroelastic problems is revealed by the two diagrams in Fig. 8.12. In the upper diagram the vertical bending deformations of the MDO wing, as predicted by the eight methods mentioned before, are plotted. They show, despite the complexity of the problem, surprisingly good agreement for the trailing edge as well as the leading

[22] MDO $\Longrightarrow$ Multidisciplinary Design Optimization.

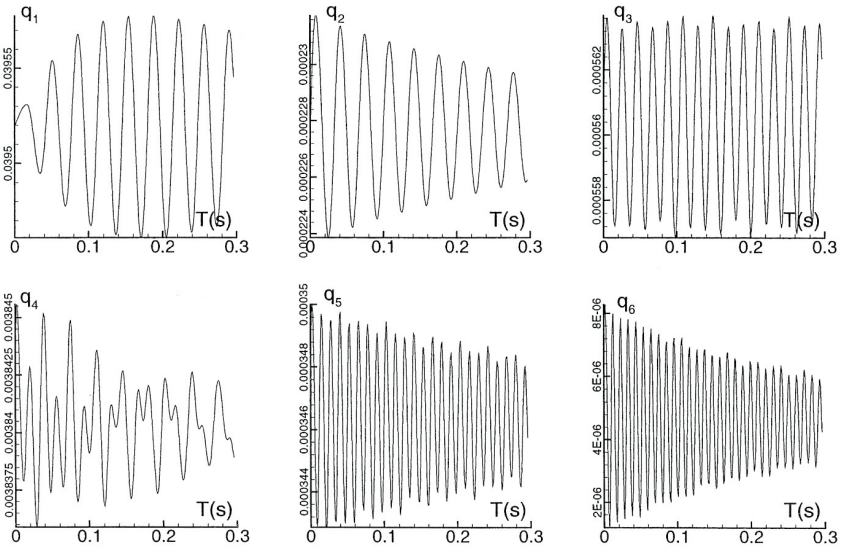

Fig. 8.10. AMP wing: dynamic aeroelastic solution [39]. Flow field found with Euler code CANARI. Time evolution of the six first modal coordinates q_i. $M_\infty = 0.78$, $\alpha = 1.79^\circ$, $p_{stag} = 90$ kPa, $Re = 3.49 \cdot 10^6$, $C_L = 0.3$.

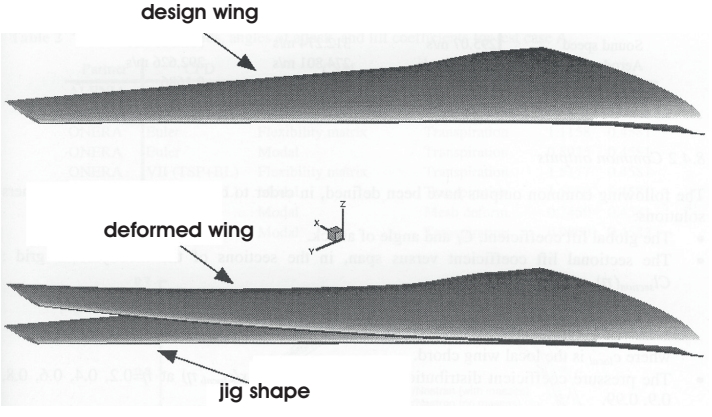

Fig. 8.11. MDO wing: static aeroelastic solution [39]. Jig shape definition with ONERA's inviscid-viscous interaction code VIS25. Design flight conditions: $M_\infty = 0.85$, flight altitude $H = 11,280$ m, total aircraft lift $C_L = 0.458$.

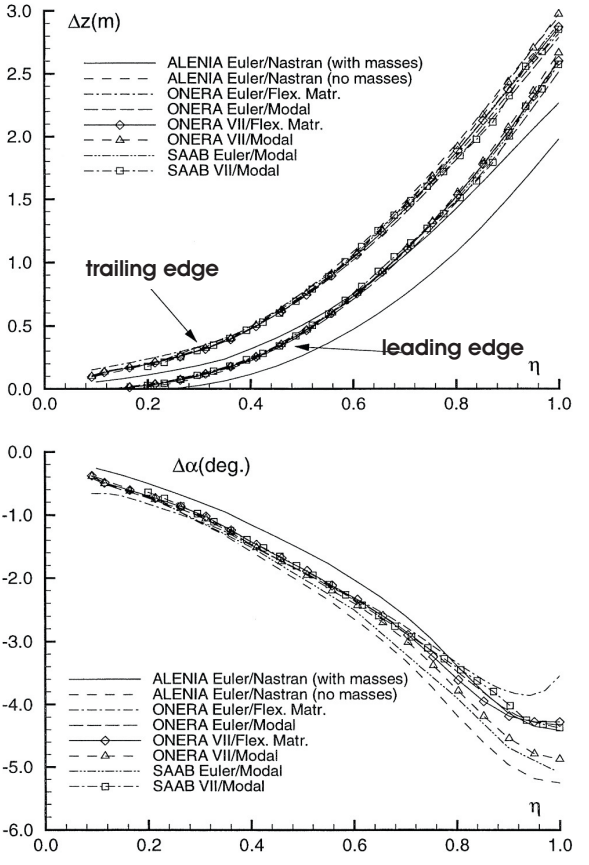

Fig. 8.12. MDO wing: static aeroelastic solution [39]. Spanwise leading and trailing edge deflection Δz (above) as well as twist deformation $\Delta\alpha$ (below). Design flight conditions: $M_\infty = 0.85$, flight altitude $H = 11,280$ m, total aircraft lift $C_L = 0.458$.

edge deflections. Note, that the deflection amounts to approximately 3 m at the wing tip for a wing half-span of 37.5 m. The predictions of the twist deformation versus span (lower part of Fig. 8.12) agree well in the inner part of the wing, whereas at the tip larger differences appear, which we have similarly identified also in Fig. 8.9 (right).

Turning to simulations of the dynamic aeroelasticity of the MDO wing, two test conditions, apart from the optimized cruise conditions, were defined. For these the Mach number is $M_\infty = 0.88$, and in the first case the altitude amounts to $H = 7$ km, corresponding to a dynamic pressure $q_\infty = 22.25$ kPa, and in the second case the altitude is $H = 2$ km, corresponding to $q_\infty = 43.10$ kPa.

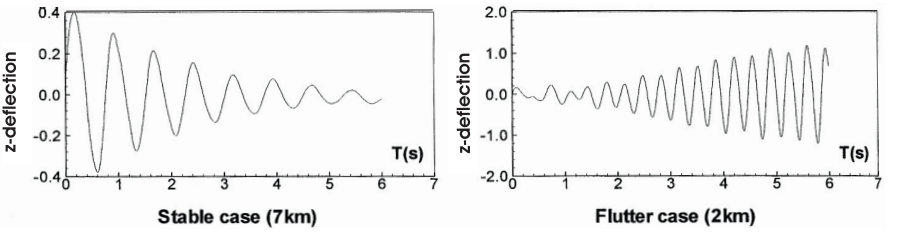

Fig. 8.13. MDO wing: dynamic aeroelastic solution (Euler solution by SAAB), [39]. z-deflection time series for a stable case at the flight altitude $H = 7$ km (left), and for a flutter case at the flight altitude $H = 2$ km (right). $M_\infty = 0.88$.

Four institutions (three industrial companies, one research institute) delivered results of six different methods for these test cases. The structural analysis is represented by a modal approach taking into account the twenty lowest wing-normal vibration modes. All the simulations predict for the $H = 7$ km case a damping of the excitations (stable flight) and for the $H = 2$ km case an increase of the oscillations (flutter response). As an example, Fig. 8.13 shows the time evolution of the deflection of the leading edge at 99 per cent half span. For the reader interested in more details, we refer to [39, 40].

8.4.3 Thermal–Fluid–Structure Interaction

In Sub-Section 8.3.3, we have discussed the description of thermal–mechanical fluid–structure interactions characterized by a mechanical response in the form of mechanical and thermal stresses. In this Sub-Section we look now at interaction cases without mechanical response. Two cases with mechanical response are presented in Sub-Section 8.4.4.

Let us consider a winged aerospace vehicle. We are concerned with the question at what locations and under what conditions thermal fluid-structure interactions play a role. As we know from Chapters 3 to 6, the thermal loads are particularly high at forward stagnation points, along leading edges of wings, fins and winglets, at deflected aerodynamic control surfaces, and in regimes where a strong expansion of the flow leads to a drastic reduction of the boundary layer thickness (e.g., shoulder of capsules, Chapter 5).

What we also know is that at a surface part with small contour radius/radii the heat flux in the gas at the wall, q_{gw}, is larger than for the case with large radius/radii[23] [5]. If the vehicle surface is radiation cooled, which is the rule, this holds also for the wall temperature. However, this temperature then drops surface-tangentially very fast with increasing running length s of the boundary layer, and so does the heat flux in the gas at the wall.

High temperatures at strongly curved surfaces and strong temperature gradients in the surface-tangential direction, lead to a special phenomenon, viz.

[23] On a sphere we have $q_{gw} \sim 1/\sqrt{R}$, Section 10.3.

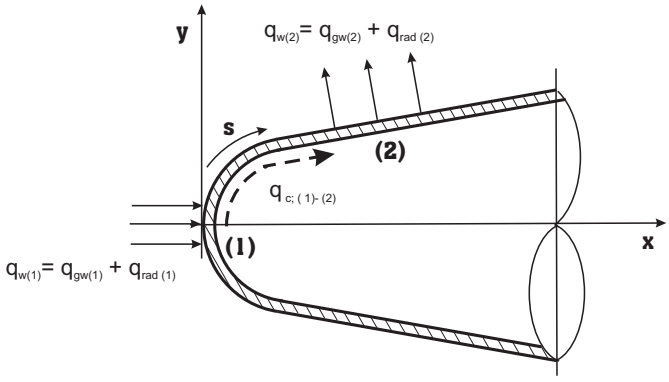

Fig. 8.14. Sketch of tangential heat transport $q_{c;(1)-(2)}$ by conduction inside a structural shell (hot primary structure of a nose cone). It diminishes the temperature at the stagnation point (1) and increases the temperature more downstream (2), leading there to a higher surface heat radiation $q_{rad(2)}$.

heat transport by conduction tangentially through the structure. This is indicated at the shape shown in Fig. 8.14, representing the hot primary structure of a nose cone. Heat is conducted from location (1) to location (2), consequently the wall temperature at location (1) is reduced, whereas it is increased at location (2). As a result less heat is radiated away at (1) and more at (2) than would be the case if the surface material did not allow any tangential heat conduction.

Hence we can say that in regions with strong tangential heat conduction within the structure the surface-temperature distribution along the surface coordinate is smoothed out to some extent. With increasing curvature the effect is getting stronger. Accordingly we must note, that in such regimes on a flight vehicle, Fig. 8.15, the radiation-adiabatic wall temperature gradually is no more an adequate approximation of the actual surface temperature.

Similar effects can be observed in gaps, existing for example around the hinge area of flaps, elevons, et cetera. Turning to the heating of deflected aerodynamic control surfaces, in our case the body flaps of the X-38 vehicle, Fig. 8.16, we are confronted with the situation that the wall thermal flux $q_w = q_{gw} + q_{rad}$ (the value is negative for heat transferred into the structure!) conducts heat from the wind side to the lee side of the flap—transverse heat transport, Sub-Section 6.3.3—and radiates into the cavity, heating up strongly the lower side of the fuselage. For all these problems a coupled thermal fluid-structure simulation is indispensable, otherwise the thermal loads and the thermal state of the surface could be predicted with dramatic errors.

We now study quantitatively the situation of tangential heat transport at the two-dimensional representation of the leading edge of a hypersonic flight vehicle [53], like the SÄNGER lower stage, Chapter 4. In Fig. 8.17 (upper part)

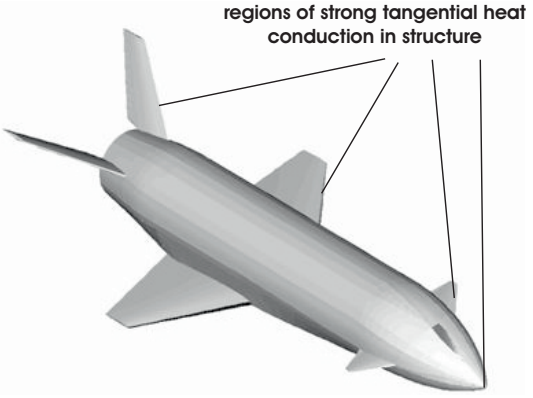

Fig. 8.15. Regimes on an aerospace vehicle with potentially strong thermal–fluid–structure interactions.

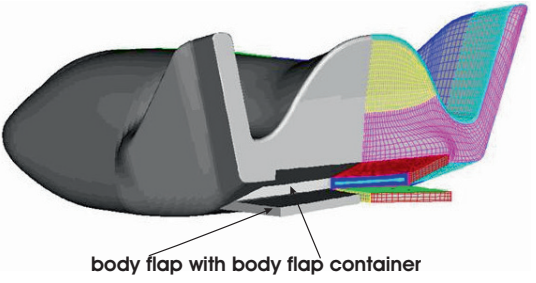

Fig. 8.16. X-38, view from behind showing the deflected body flaps with the body flap container as part of the fuselage. The right part of the figure shows the surface grid for flow computation.

we find details of the geometry and the structure of the leading edge. For the nose radius $R_2 = 4$ mm, temperature contours are given in the lower part of the figure,[24] found with a coupled Navier–Stokes/FEM solution for the flight conditions $M_\infty = 6.5$ and $H = 30$ km. The coupling of the discipline codes was conducted by the Dirichlet–Neumann method, eq. (8.27), and the data at the common boundary interface were transferred by means of a virtual surface.

For different nose radii the wall temperatures in the vicinity of the stagnation point are plotted in Fig. 8.18 (upper part). As expected, the peak temperatures increase with decreasing nose radius. In addition the wall heat flux $q_w = q_{gw} + q_{rad}$ is displayed in Fig. 8.18 (lower part), showing two interesting trends. First, for large radii the wall heat flux q_w in the stagnation regime tends to zero, indicating that the wall behaves radiation-adiabatic. Second, for small

[24] The slight asymmetry of the temperature cannot be explained.

radii the wall heat flux q_w is large at the stagnation point, while heat is transferred tangentially in the structure along the coordinate s (not shown here). This leads to the effect, that some distance away from the stagnation point more heat q_{rad} is radiated from the surface than the flow is able to transport (q_{gw}) to the surface. This effect, although not very large in this case, is well discernible in Fig. 8.18 (below).

We focus now our attention on another case, the gap model, which was designed for experimental investigations of thermal loads in DLR's plasma tunnel L3K in the frame of the German technology programme TETRA,[25] [54], see also Section 6.4. In the follow-on programme ASTRA[26] intensive work was devoted to coupled thermal–mechanical fluid–structure interaction problems. The gap model, Fig. 8.19, was fitted to obtain validation data for the newly developed coupled simulation environment. This environment, used for the test case, which we will discuss below, was based on [48, 49]:

- the finite-volume τ code (DLR) for the solution of the Navier–Stokes equations on unstructured grids,
- the finite element commercial code ANSYS for the structural and thermal equilibrium mechanics computations,
- the Dirichlet–Neumann method, eq. (8.27), for the coupling of the discipline codes,
- the commercial interpolation software MpCCI [50], for the data transfer between the non-matching boundary interfaces.

The two-dimensional Navier–Stokes solution, for the test conditions of the plasma tunnel L3K with $M_\infty = 7.27$, $\alpha = 15°$, $T_\infty = 620$ K, $Re = 12.1 \cdot 10^4$, with open gap,[27] gives an impression of the topology of the streamlines, Fig. 8.20 [55]. The figure shows, that despite the fact that in reality the flow is three-dimensional, Fig. 8.21, a small vortex is created due to the flow separation at the upstream part of the gap inflow. This prevents a direct flow into the gap. The fluid material, which reaches the gap, streams around the vortex. Some of it has traveled up to an attachment point on the ramp before turning back to the gap.

The influence of the thermal–fluid–structure coupling, with non-convex effects taken into account, see also Section 6.4 and Sub-Section 6.7.2, is shown in Fig. 8.21. The comparison of the wall temperatures exhibits clearly the coupling effect. Generally, the temperatures of the coupled solution are lower than the uncoupled (radiation-adiabatic surface boundary condition) ones and this

[25] **TE**chnologien für zukünftige Raum**TRA**nsportsysteme (Technologies for Future Space Transportation Systems), 1998-2001.

[26] **A**usgewählte **S**ysteme und **T**echnologien für zukünftige **R**TS-**A**nwendungen (Selected Systems and Technologies for Future Space Transportation Systems Applications), 2001–2003.

[27] Open and closed gaps represent different states of flow, for example near the hinge line of aerodynamic control surfaces (flaps, elevons, etc), Section 6.4.

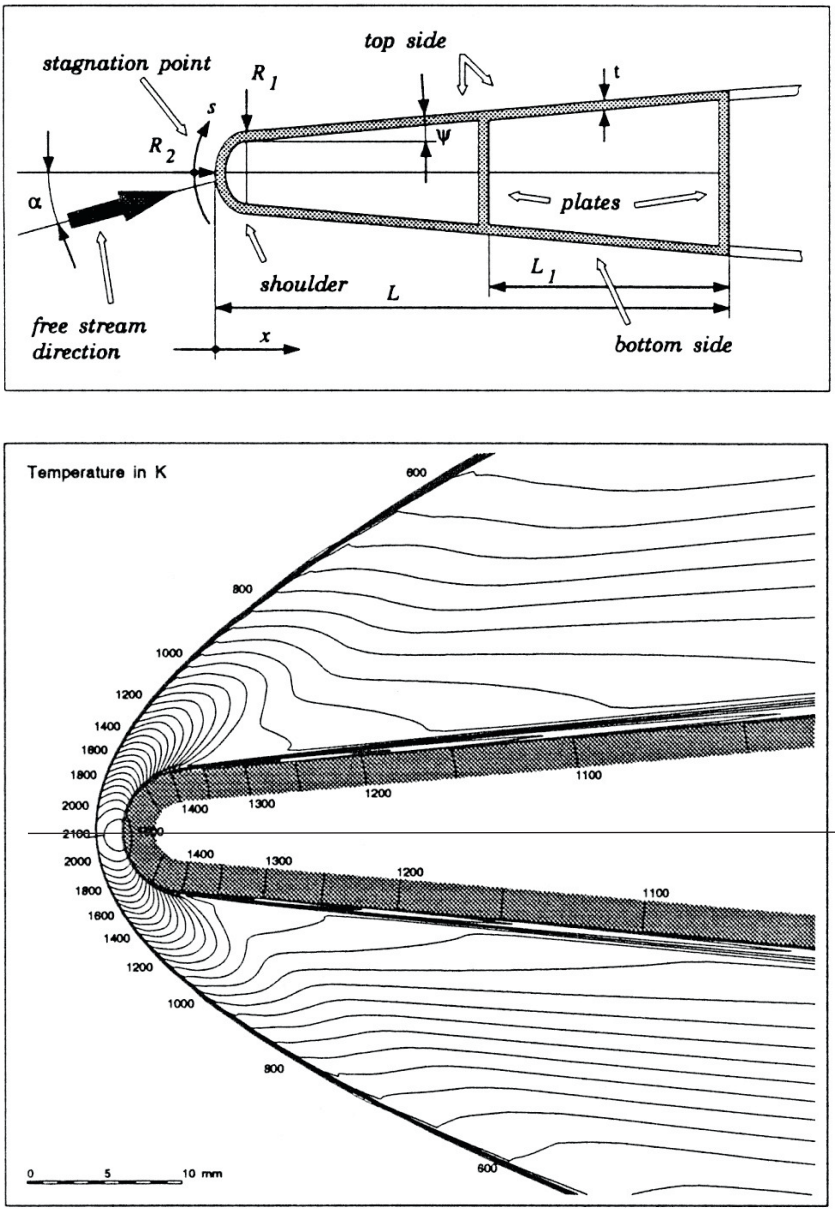

Fig. 8.17. Tangential heat transport: geometry of the 2-D leading edge test case (above), and lines of constant temperatures found with a coupled Navier–Stokes solution for $M_\infty = 6.5$ and $H = 30$ km (below), nose radius $R_2 = 4$ mm [53].

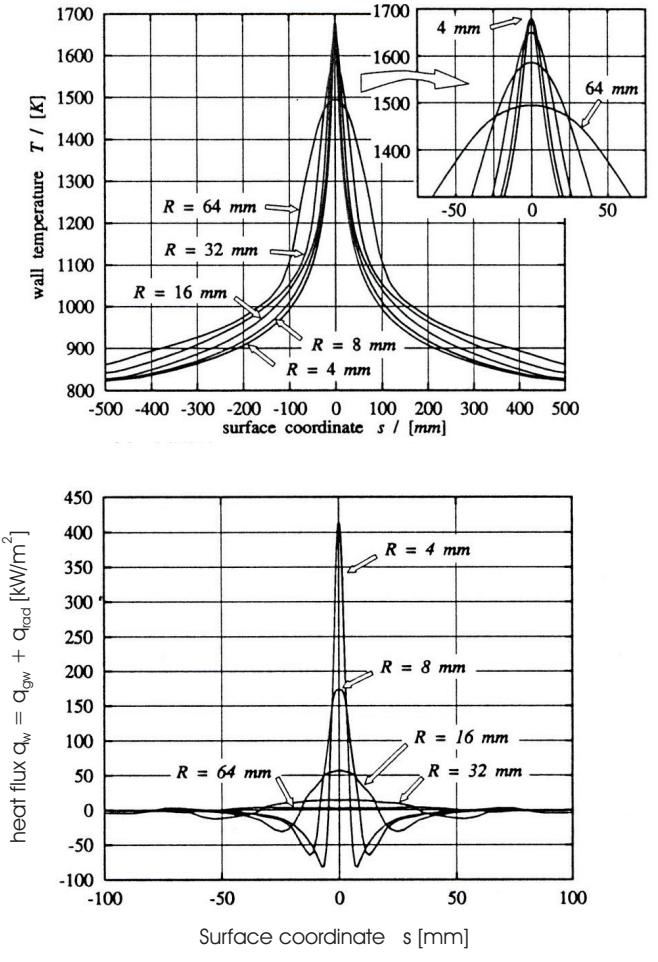

Fig. 8.18. Tangential heat transport in the structure shown in Fig. 8.17 (upper part): wall temperatures T (above) and wall heat fluxes into the structure q_w for different nose radii $R \equiv R_2$ (below) [53].

is more pronounced at the side edges and in regions with high surface curvature (e.g., gap inlet), Fig. 8.21 (left).

Wall temperatures in the symmetry plane, calculated with the coupled and the uncoupled approach, are compared with L3K plasma tunnel data in Fig. 8.21 (right). The level of the experimental data is higher than the level of the numerical ones. Further it seems that at least upstream of the gap the uncoupled data agree better with the experimental ones compared with the results of the coupled solution.

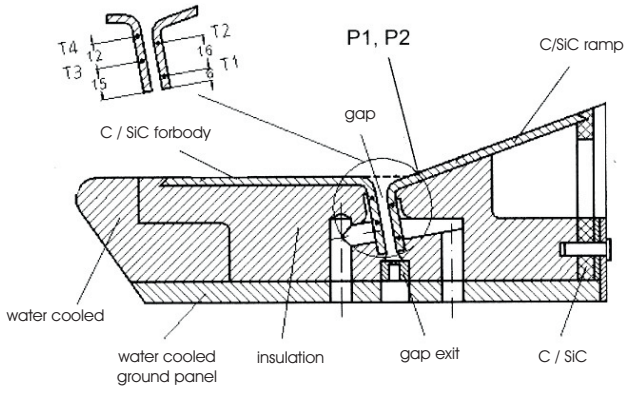

Fig. 8.19. Sketch of the configuration of the gap model [54].

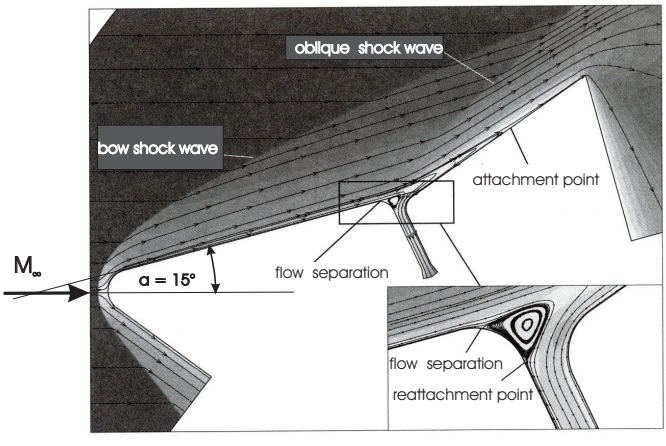

Fig. 8.20. Gap model: topology of the 2-D velocity field (streamlines) for open gap (lower right) [48, 56]. Plasma tunnel test conditions: $M_\infty = 7.27$, $\alpha = 15°$, $T_\infty = 620$ K, $Re = 12.1 \cdot 10^4$.

The next considered test case in this context is a generic body flap model, which was to model the situation at the rear of the X-38, see also Sub-Section 6.3.3. With it essentially the fluid and thermal behavior in the cavity between the lee side of the flap and the ground of the flap box (lower side of the fuselage) was investigated, Fig. 8.22. All plates of the model were manufactured from the ceramic material C/C-SiC, except for the blunt nose part, which was a water-cooled steel part.

We highlight in particular the heat conduction in the structure from the wind side to the lee side of the flap (transverse heat transfer) and the subsequent radiation exchange with the ground plate. In Fig. 8.23 the surface tem-

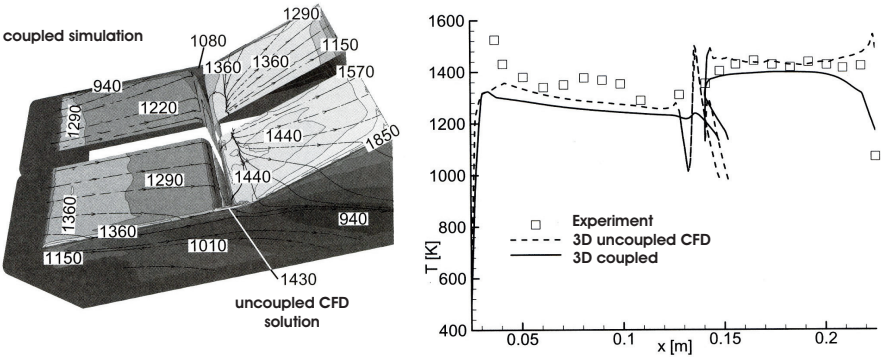

Fig. 8.21. Gap model: comparison of coupled and uncoupled (radiation-adiabatic) 3-D solution for model with open gap [48, 56]. Wall temperature distribution (left), wall temperature distribution in symmetry plane (right).

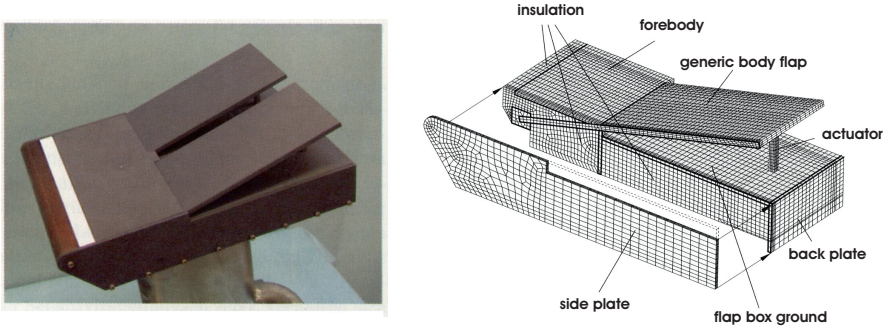

Fig. 8.22. Body flap model. Plasma tunnel model (left), sketch of the construction (right), [23, 48]. Material of the plates is C/C-SiC, and material of the insulation Al_2O_3.

peratures and the streamlines are displayed in an explosion view for the uncoupled (radiation-adiabatic surface boundary condition) and the coupled numerical simulation.

There are three main differences between the two solutions:

1. The temperatures along the boundaries of the flap and on the ground plate ('flap box ground' in Fig. 8.23) as well as at the junction between the forebody and the nose part are relatively high in the uncoupled solution. In the coupled solution these strong temperature gradients are damped out by the heat conduction in the structure. This leads to more homogeneous wall temperature fields.

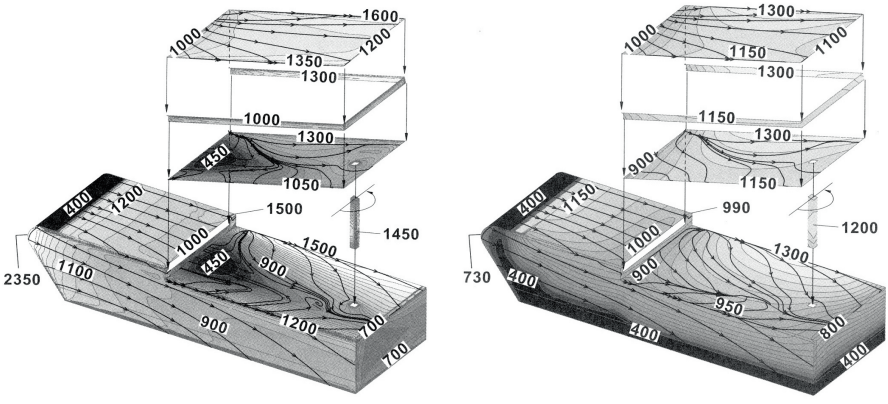

Fig. 8.23. Surface temperatures and streamlines on the body flap model. Radiation-adiabatic (uncoupled) solution (left), coupled solution (right), [23, 48, 57]; $M_\infty = 7.36$, $\alpha = 10°$, $T_\infty = 552$ K, $Re = 11.9 \cdot 10^4$.

2. The lee side of the flap has higher wall temperatures in the coupled solution compared to the uncoupled one due to the intensive transverse heat conduction from the wind side to the lee side.
3. The wall temperature level at the ground plate in the coupled solution (except at the side edges) is increased by the heat radiation from the lee side of the flap. Note in this context also the changes of the topology of the skin-friction lines.

Finally we consider the surface temperature along the middle section of the flap and the ground plate ($y = 50$ mm), Fig. 8.24. Compared are the uncoupled and the coupled solutions with the experimental data. The experimental data on the wind side were obtained with an infrared imaging system whereas on the ground plate thermocouples were used. As before on the gap model the results of the uncoupled simulation for the wind side are closer to the experimental data than the coupled ones. The temperature level on the ground plate of the uncoupled solution is relatively low, what we already mentioned, but increases remarkably in the coupled simulation. The agreement of the data from this solution with the thermocouple data is more convincing than that with the infrared imaging data discussed before.

In order to assess the quality of the experimental and numerical data one should have the following in mind:

- First, such hypersonic, high-enthalpy flow situations are probably the most challenging ones from a physical point of view.
- Second, there are likely uncertainties in the experiment, stemming from, e.g., the "free-stream" produced by the conical nozzle, the heat absorbtion and emission from the tunnel walls, the homogeneity of the onset flow, the degree of chemical and thermal non-equilibrium of the gas, the gas pollution by the

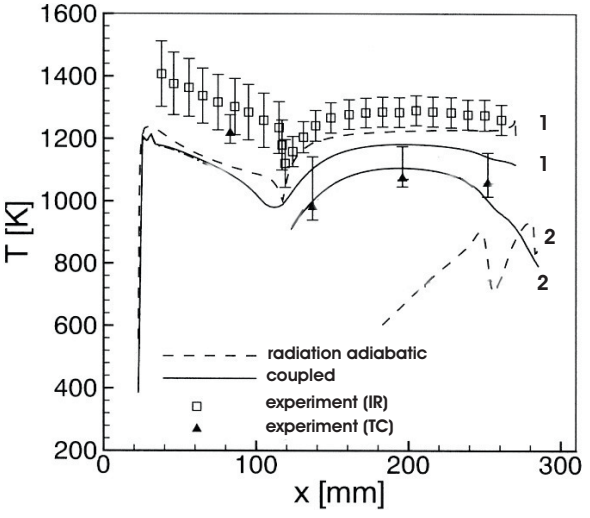

Fig. 8.24. Surface temperatures along the middle section of the flap ($y = 50$ mm), comparison of results of radiation-adiabatic and coupled simulations with experimental data [23]; $M_\infty = 7.36$, $\alpha = 10^\circ$, $T_\infty = 552$ K, $Re = 11.9 \cdot 10^4$; 1 denotes the windward side of the flap, 2 the ground plate of the flap box.

heating system of the tunnel, the accuracy of the measurement methods, in particular of the infrared imaging system, and others. Laminar–turbulent transition is very unlikely because of the low experimental Reynolds number.

- Third, the uncertainties in the numerical simulation of the flow field, e.g., in the modelling of the catalytic effects at the wall, of the chemical and thermal non-equilibrium effects, of the wall radiation effects including non-convex effects, the accuracy of the interpolation along the interface boundary, and others.

8.4.4 Thermal–Mechanical–Fluid–Structure Interaction

We present here a result of probably the first work [42] which dealt with a coupled thermal–mechanical fluid–structure interaction problem, as formulated in Sub-Section 8.3.3. A thin panel is considered, which is fixed in a panel holder, which is declined by an angle $\alpha = 15^\circ$ to the free-stream with $M_\infty = 6.57$, and $Re^u = 1.214 \cdot 10^6$ m^{-1}, Fig. 8.25 a). The oblique shock produces a boundary layer flow with a Mach number $M_\infty = 4.24$, and a unit Reynolds number $Re^u = 2.16 \cdot 10^6$ m^{-1} , Fig. 8.25 b). All the sets of equations, given in Sub-Section 8.3.3 for the flow, the structure and the heat conduction in the solid are solved by using the finite element approach.

Due to the grid-point coincidence along the common boundary interface no interpolation was necessary for the data transfer. The coupled simulation was

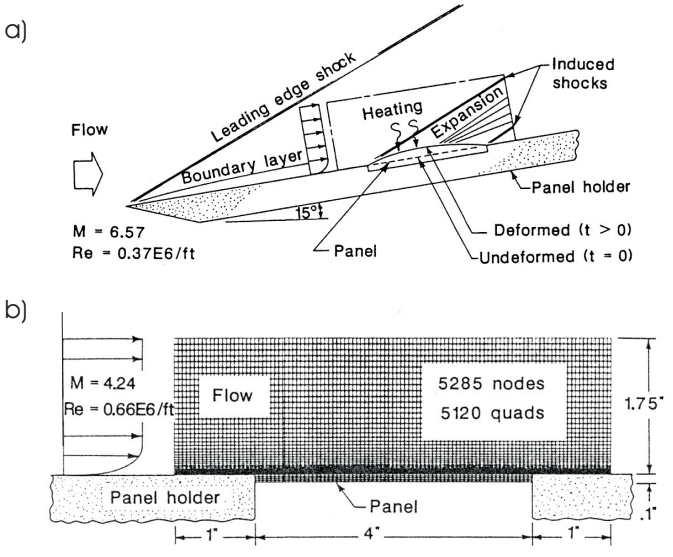

Fig. 8.25. Flow over a panel fixed in a panel holder [42]. Coupled thermal–mechanical fluid–structure finite element model, panel holder inclination $\alpha = 15°$, free-stream conditions $M_\infty = 6.57$, $Re^u = 1.214 \cdot 10^6$ m^{-1}, upper figure a), and panel onset-flow conditions $M_\infty = 4.24$, $Re^u = 2.16 \cdot 10^6$ m^{-1}, lower figure b).

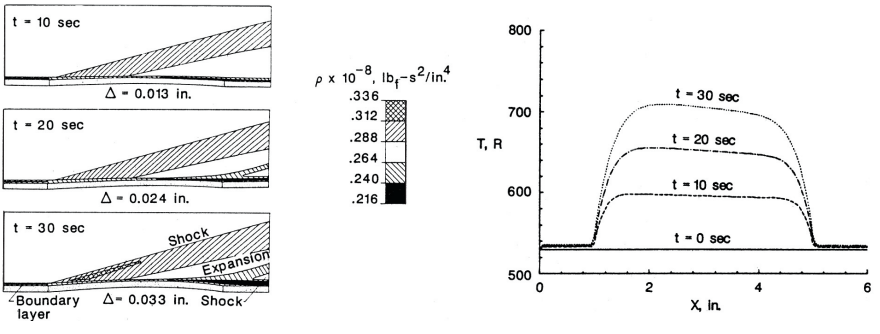

Fig. 8.26. Flow over a panel fixed in a panel holder [42]. Panel deformation and density distribution (left), wall temperature distribution (right), $M_\infty = 4.24$, $\alpha = 15°$, $Re = 2.16 \cdot 10^6$.

carried out for a time period of 30 s, where the system was yet in a transient phase. Equilibrium was estimated for times larger than 600 s.

We show in Fig. 8.26 for the first 30 s the time evolution of the deformation of the panel and the density distribution (left), as well as the wall temperature distribution (right). The temperature profiles reflect also the influence of the heat transfer into the cooled panel holder.

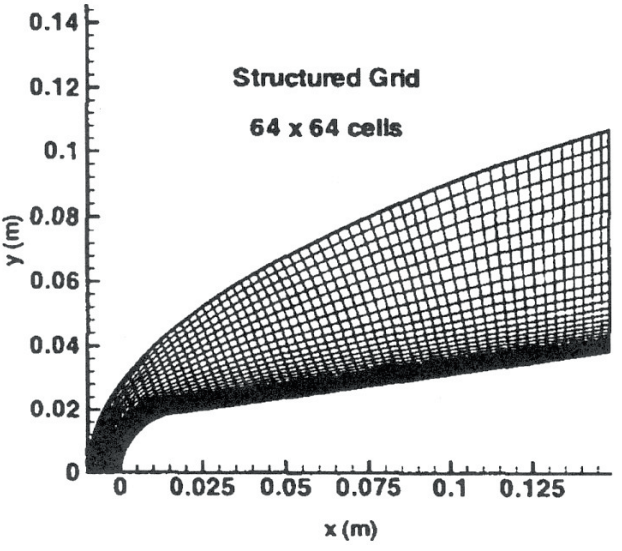

Fig. 8.27. Sphere-cone nose of a re-entry test vehicle, geometry and grid in the fluid domain [58].

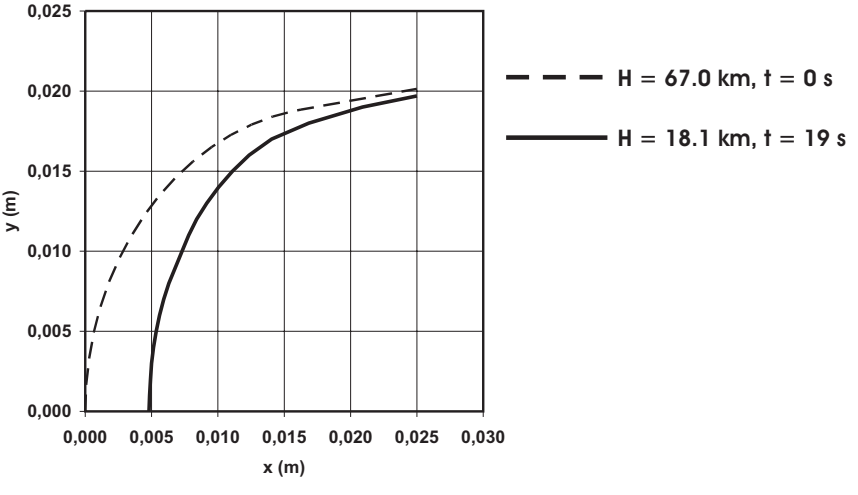

Fig. 8.28. Sphere-cone nose of a re-entry test vehicle [59]. Ablated nose shape after a flight along a re-entry trajectory of 19 s.

The same problem was treated with the more advanced coupling environment reported in [43]. Again the sets of equations were solved by finite element approaches, but in an iterative way (loosely coupled algorithm). Since different mesh sizes were used in the fluid and the structural domain, the data transfer at the interface boundary was conducted by interpolation via a virtual surface.

As a last example we consider the case of a thermal-mechanical fluid-structure interaction with ablation [58, 59]. Ablating materials are often employed on expendable RV-NW's (re-)entering the atmosphere, e.g., capsules. The theoretical treatment of ablation requires a complex multi-phase physical and chemical modeling. In the fluid domain a thermal-chemical non-equilibrium Navier–Stokes code on finite-volume basis was used, which is able to consider in the chemical model also the species from the ablated material injected into the air. On the structural side a generalized finite element code for solving diffusion problems was applied to determine the heat conduction in the solid. This code includes the capability to update the structural grid which is changed due to the mass loss rate of ablation. To avoid complex interpolations, the meshes of the different domains have coincident nodes on the interface boundary. With the displacements provided by the structural code an updated mesh in the fluid domain was calculated.

A sphere-cone configuration as part of a simple space vehicle was investigated axisymmetrically, Fig. 8.27. The ablating material was carbon-carbon. Ballistic flight was simulated from the altitude $H = 67$ km down to $H = 18.1$ km for a duration of 19 s. Figure 8.28 shows the computed change of shape in the nose regime owing to ablation.

8.5 Conclusion

Multidisciplinary simulation and optimization is a relatively young branch in particular for the flow, the structure, and the heat conduction disciplines in combination with advanced numerical simulation methods. Of course, theoretical investigations of the aeroelasticity of airplanes or parts of airplanes have a long tradition, but in the earlier days the theoretical approach was usually based on analytical solutions. With the advent of high-performance computers and competitive computer codes for the numerical simulation of various disciplines, this situation has changed. Now we observe the trend that simulation environments for a coupled treatment of:

- mechanical fluid-structure (aeroelastic, static and dynamic (flutter), aeroacustics),
- thermal fluid-structure (aerothermal, quasi-steady),
- thermal-mechanical fluid-structure (aerothermoelastic, quasi-steady)

interactions are developed.

Any work on the creation of simulation codes needs data for the verification of the methods. These data can come from experiments, free flights or from

other theoretical simulation methods. Often such data are barely available. Helpful for our discussions in Section 8.4 were data from the project IMENS,[28] where Germany's DLR together with the industry (EADS-ST) combined experimental and theoretical work in that field [23],[45]-[49].

The quality of the experimental and theoretical data are not in all aspects satisfactory, but the knowledge about the possible drawbacks and influences has a good basis and was further advanced after the end of the project. Looking at the worldwide ongoing efforts, it can be expected that in the near future the methods of multidisciplinary design and optimization will become accurate and reliable tools for the design and development of aerospace flight vehicles.

8.6 Problems

Problem 8.1 Consider expansion of air as perfect gas with a total temperature $T_t = 1,500$ K. How large is the maximum possible speed V_m?

Problem 8.2. Prove that the formulations eqs. (8.2) and (8.8) are identical by employing the unsteady, two-dimensional inviscid part of these equations. It is sufficient to consider one component, for example the continuity equation.

Problem 8.3. The radiation-adiabatic temperature at a spherical nose with radius R is proportional to $R^{-0.125}$ [5]. We can determine this also from Section 10.3 when putting $q_{gw} \sim T_{ra}^4$ into the relations given there. Apply this to the results shown in the upper part of Fig. 8.18. Take as reference case the case with $R = 64$ mm, where the tangential heat transfer is small and the wall temperature can be considered approximately as radiation-adiabatic, obtain results for the smaller radii, and compare with the data in the figure.

Problem 8.4 We have learned in this chapter that a thermal–mechanical coupling exists between aerothermodynamics and the structure of aerospace vehicles flying with high Mach numbers. We found that this coupling is strong in forward stagnation point regions, at leading edges of wings, winglets and tails and at body flaps which are located totally or partly underneath of a fuselage. At other parts of the vehicle structure only a weak coupling is observed, and the wall temperature there is close to the radiation-adiabatic temperature.

On CAV's or ARV's with their airbreathing propulsion systems (see Figs. 4.5 and 4.14), consisting of the three main parts inlet, combustion chamber (burner) and expansion nozzle, the outer flow field is very complex, particularly with respect to the aerodynamic forces and moments as well as to the thermal loads on some surface elements. It is obvious that at some of the main parts of the propulsion system strong thermal-mechanical fluid-structure interactions occur. Indicate two of them.

[28] "Integrated Multidisciplinary Design of Hot Structures for Space Vehicles".

References

1. Anderson Jr., J.D.: The Airplane – A History of Its Technology, AIAA, Reston (2002)
2. Hirschel, E.H.: Towards the Virtual Product in Aircraft Design? In: Periaux, J., Champion, M., Gagnepain, J.-J., Pironneau, O., Stouflet, B., Thomas, P. (eds.) Fluid Dynamics and Aeronautics New Challenges. CIMNE Handbooks on Theory and Engineering Applications of Computational Methods, Barcelona, Spain, pp. 453–464 (2003)
3. Vos, J.B., Rizzi, A., Darracq, D., Hirschel, E.H.: Navier–Stokes Solvers in European Aircraft Design. Progress in Aerospace Sciences 38, 601–697 (2002)
4. Hirschel, E.H.: Historical Perspective on Programs, Vehicles and Technology Issues. In: Proc. RTO/AVT/VKI Lecture Series AVT-116 Critical Technologies for Hypersonic Vehicle Development, Rhode-Saint-Gènèse, Belgium, May 10-14. RTO-EN-AVT-116, pp. 1-1–1-22 (2005)
5. Hirschel, E.H.: Basics of Aerothermodynamics. Progress in Astronautics and Aeronautics, AIAA, Reston, Va, vol. 204. Springer, Heidelberg (2004)
6. Hammond, W.E.: Space Transportation: A System Approach to Analysis and Design. AIAA Educations Series, Reston, Va (1999)
7. Hajela, P.: Soft Computing Multidisciplinary Aerospace Design – New Directions for Research. RTO MP-35, paper 17 (1999)
8. Alexandrov, N., Hussaini, Y. (eds.): Multidisciplinary Design Optimization: State of the Art. SIAM Publications, Philadelphia (1992)
9. Haykin, S.: Neural Networks – A Comprehensive Foundation. Macmillan Publishing Company, Englewood (1994)
10. Hajela, P.: Neural Networks – Applications in Modeling and Design of Structural Systems. CISM Lecture Notes, Udine, Italy (1998)
11. Zadeh, L.: Fuzzy Sets. Information and Control 8, 338–353 (1965)
12. Yuan, W.G., Quan, W.W.: Fuzzy Optimum Design of Structures. Engineering Optimization 8, 291–300 (1985)
13. Haftka, R.T., Gurdal, Z.: Elements of Structural Optimization. Kluwer Academic Publishers, Dordrecht (1993)
14. Hajela, P., Yoo, J.: Constraint Handling in Genetic Search Using Expression Strategies. AIAA Journal 34(11), 2414–2420 (1996)
15. Aris, R.: Vectors, Tensors and the Basic Equations of Fluid Mechanics. Prentice Hall, Englewood Cliffs (1962)
16. Farhat, C., Lesoinne, M., Chen, P.S.: Parallel Heterogeneous Algorithms for the Solution of Three-Dimensional Transient Coupled Aeroelastic Problems. AIAA-Paper 95-1290 (1995)
17. Lesoinne, M., Farhat, C.: Geometric Conservation Laws for Aeroelastic Computations Using Unstructured Dynamic Meshes. AIAA-Paper 95-1709-CP (1995)
18. Farhat, C., Lesoinne, M.: Higher-Order Staggered and Subiteration Free Algorithms for Coupled Dynamic Aeroelasticity Problems. AIAA-Paper 98-0516 (1998)
19. Farhat, C., Lesoinne, M., LeTallec, P.: Load and Motion Transfer Algorithms for Fluid/Structure Interaction Problems with Non-Matching Discrete Interfaces: Momentum and Energy Conservation, Optimal Discretisation and Application to Aeroelasticity. Comput. Methods Appl. Mech. Eng. 157, 95–114 (1998)

20. Gupta, K.K., Meek, J.L.: Finite Element Multidisciplinary Analysis. AIAA Education Series, Reston, Va (2000)
21. Zienkiewics, O.C., Taylor, R.L., Zhu, J.Z.: Finite Element Method: Its Basis and Fundamentals. Elsevier Butterworth-Heinemann, New York (2005)
22. Bathe, K.J.: Finite Element-Methoden. Springer, Heidelberg (2002)
23. Schäfer, R.: Thermisch-mechanisches Verhalten heisser Strukturen in der Wechselwirkung mit einem umströmenden Fluid (Thermo-Mechanical Behavior of Hot Structures in Interaction with a Fluid). Doctoral Thesis, Technische Universität Stuttgart, Germany, DLR Forschungsbericht 2005 - 02 (2005)
24. Gupta, K.K., Petersen, K.L., Lawson, C.L.: On Some Recent Advances in Multidisciplinary Analysis of Hypersonic Vehicles. AIAA-Paper 92-5026 (1992)
25. Gupta, K.K.: Development of a Finite Element Aeroelastic Analysis Capability. Journal of Aircraft 33(5), 995–1002 (1996)
26. Cowan, T.J., Arena Jr., A.S., Gupta, K.K.: Accelerating CFD-Based Aeroelastic Predictions Using System Identification. AIAA-Paper 98-4152 (1998)
27. Cowan, T.J., Arena Jr., A.S., Gupta, K.K.: Development of a Discrete-Time Aerodynamic Model for CFD-Based Aeroelastic Analysis. AIAA-Paper 99-0765 (1999)
28. Gupta, K.K., Voelker, L.S., Bach, C., Doyle, T., Hahn, E.: CFD-Based Aeroelastic Analysis of the X-43 Hypersonic Flight Vehicle. AIAA-Paper 2001-0712 (2001)
29. Gupta, K.K., Bach, C., Doyle, T., Hahn, E.: CFD-Based Aeroservoelastic Analysis with Hyper-X Applications. AIAA-Paper 2004-0884 (2004)
30. Maute, K., Nikbay, M., Farhat, C.: Analytically Based Sensitivity Analysis and Optimization of Nonlinear Aeroelastic Systems. AIAA-Paper 2000-4825 (2000)
31. Tran, H., Farhat, C.: An Integrated Platform for the Simulation of Fluid-Structure-Thermal Interaction Problems. AIAA-Paper 2002-1307 (2002)
32. Selmin, V.: Coupled Fluid-Structure System. In: Haase, W., Selmin, V., Wingzell, B. (eds.) Progress in Computational Flow-Structure Interactions. Notes on Numerical Fluid Mechanics and Multidisciplinary Design, vol. 81, pp. 13–20. Springer, Heidelberg (2003)
33. Patel, A., Hirsch, C.: All-hexahedra Unstructured Flow Solver for External Aerodynamics with Application to Aeroelasticity. In: Haase, W., Selmin, V., Wingzell, B. (eds.) Progress in Computational Flow-Structure Interactions. Notes on Numerical Fluid Mechanics and Multidisciplinary Design, vol. 81, pp. 105–116. Springer, Heidelberg (2003)
34. Dervieux, A., Koobus, B., Schall, E., Lardat, R., Farhat, C.: Application of Unsteady Fluid-Structure Methods to Problems in Aeronautics and Space. In: Barton, N.G., Periaux, J. (eds.) Coupling of Fluids, Structures and Waves in Aeronautics. Notes on Numerical Fluid Mechanics and Multidisciplinary Design, vol. 85, pp. 57–70. Springer, Heidelberg (2003)
35. Maman, N., Farhat, C.: Matching Fluid and Structure Meshes for Aeroelastic Computations: A Parallel Approach. Computer & Structures 54, 779–785 (1995)
36. Löhner, R.: Robust, Vectorized Search Algorithms for Interpolation of Unstructured Grids. J. of Comp. Phys. 118, 380–387 (1995)
37. Grashof, J., Haase, W., Schneider, M., Schweiger, J., Stettner, M.: Static and Dynamic Aeroelastic Simulations in Transonic and Supersonic Flow. In: Haase, W., Selmin, V., Wingzell, B. (eds.) Progress in Computational Flow-Structure Interactions. Notes on Numerical Fluid Mechanics and Multidisciplinary Design, vol. 81, pp. 39–46. Springer, Heidelberg (2003)

38. Lepage, C.H., Habashi, W.G.: Conservative Interpolation of Aerodynamic Loads for Aeroelastic Computations. AIAA-Paper 2000-1449 (2000)
39. Haase, W., Selmin, V., Wingzell, B. (eds.): Progress in Computational Flow-Structure Interactions. Notes on Numerical Fluid Mechanics and Multidisciplinary Design, vol. 81. Springer, Heidelberg (2003)
40. Barton, N.G., Periaux, J. (eds.): Coupling of Fluids, Structures and Waves in Aeronautics. Notes on Numerical Fluid Mechanics and Multidisciplinary Design, vol. 85. Springer, Heidelberg (2003)
41. Ballmann, J.: Flow Modulation and Fluid-Structure Interaction at Airplane Wings. Notes on Numerical Fluid Mechanics and Multidisciplinary Design, vol. 84. Springer, Heidelberg (2003)
42. Thornton, E.A., Dechaumphai, P.: Coupled Flow, Thermal, and Structural Analysis of Aerodynamically Heated Panels. J. of Aircraft 25(11), 1052–1059 (1988)
43. Löhner, R., Yang, C., Cebral, J., Baum, J.D., Luo, H., Pelessone, D., Charman, C.: Fluid-Structure-Thermal Interaction Using a Loose Coupling Algorithm and Adaptive Unstructered Grids. AIAA-Paper 98-2419 (1998)
44. Haupt, M., Horst, P.: Coupling of Fluid and Structure Analysis Codes for Air- and Spacecraft Applications. In: Bathe, K.J. (ed.) Proceedings First MIT Conference on Computational Fluid and Solid Mechanics. Computational Fluid and Solid Mechanics, pp. 1226–1231. Elsevier, Amsterdam (2001)
45. Haupt, M., Niesner, R., Horst, P.: Flexible Software Environment for the Coupled Aerothermodynamic-Thermal-Mechanical Analysis of Structures. ESA SP-563 (2005)
46. Schäfer, R., Mack, A., Esser, B., Gülhan, A.: Fluid-Structure Interaction on a Generic Model of a Reentry Vehicle Nosecap. In: Librescu, L., Marzocca, P. (eds.) Proceedings 5th International Congress on Thermal Stresses and Related Topics. Blacksburg, Virginia (2003)
47. Haupt, M., Niesner, R., Unger, R., Horst, P.: Computational Aero-Structural Coupling for Hypersonic Applications. AIAA Paper 2006-3252 (2006)
48. Mack, A.: Analyse von heissen Hyperschallströmungen um Steuerklappen mit Fluid-Struktur Wechselwirkung (Analysis of Hot Hypersonic Flow Past Control Surfaces with Fluid-Structure Coupling). Doctoral Thesis, Technische Universität Braunschweig, Germany, DLR Forschungsbericht 2005 - 23 (2005)
49. Haupt, M., Niesner, R., Horst, P., Hannemann, V., Mack, A., Brandl, A.: Numerical and Software Concepts for the Coupling of Structural Thermal-Mechanical and Fluid-Dynamic Codes. In: Librescu, L., Marzocca, P. (eds.) Proceedings 5th International Congress on Thermal Stresses and Related Topics. Blacksburg, Virginia (2003)
50. N.N.: MpCCI, Mesh-based parallel Code Coupling Interface, Specification of MpCCI Version 1.3. Fraunhofer Institute for Algorithm and Scientific Computing SCAI (2002)
51. Weiland, C.: Stage Separation Aerothermodynamics. AGARD-R-813, pp. 11-1–11-28 (1996)
52. Gupta, K.K.: Development and Application of an Integrated Multidisciplinary Analysis Capability. International Journal for Numerical Methods in Engineering 40, 533–550 (1997)
53. Haupt, M., Kossira, H.: Analysis of Structures in Hypersonic Fluid Flow Including the Fluid-Structure Interaction. ESA SP-428 (1998)

54. Gülhan, A.: Investigation of Gap Heating on a Flap Model in the Arc Heated Facility L3K. Deutsches Zentrum für Luft- und Raumfahrt, TETRA Programme, TET-DLR-21-TN-3101 (1999)
55. Behr, R., Görgen, J.: CFD Analysis of Gap Flow Phenomena. Deutsches Zentrum für Luft- und Raumfahrt, TETRA Programme, TET-DASA-21-TN-2403 (2000)
56. Mack, A., Schäfer, R.: Fluid Structure Interaction on a Generic Body-Flap Model in Hypersonic Flow. J. of Spacecraft and Rockets 42(5), 769–779 (2005)
57. Esser, B., Gülhan, A., Schäfer, R.: Experimental Investigation of Thermal Fluid – Structure Interaction in High Enthalpy Flow. ESA SP-563 (2005)
58. Kuntz, D.W., Hassan, B., Potter, D.L.: An Iterative Approach for Coupling Fluid/Thermal Predictions of Ablating Hypersonic Vehicles. AIAA-Paper 99-3460 (1999)
59. Hassan, B., Kuntz, D.W., Salguero, D.E., Potter, D.L.: A Coupled Fluid/Thermal/Flight Dynamics Approach for Predicting Hypersonic Vehicle Performance. AIAA-Paper 2001-2903 (2001)